The Imperial College of Science, Technology and Medicine

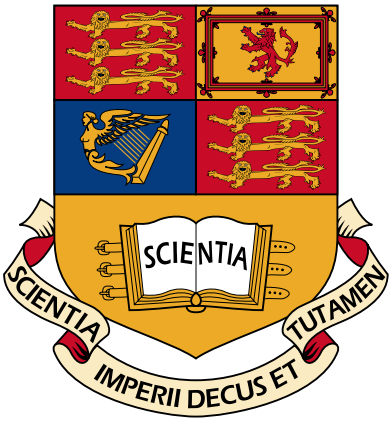

Thesis

Transition of Spatially Localised States in Shear Flows

Author:
Rishabh Gvalani

Supervisor:
Dr. Cédric Beaume

September 7, 2015

Department of Aeronautics
Imperial College London
South Kensington Campus
London SW7 2AZ, UK

And now we rise.
And we are everywhere.

– Nick Drake (1971)

Acknowledgements

First off, I would like to thank my supervisor, Dr. Cédric Beaume, who has been incredibly supportive and encouraging over the past four months. He has given me the opportunity to learn so much and for that I am grateful. I would like to thank John F. Gibson from the University of New Hampshire for providing us with the initial solutions and helping us set up Channelflow. I would also like to acknowledge Jan Niklas Rose for providing me with the LaTeX template for my thesis.

On a personal note, I want to express my deepest gratitude to my parents and family who have helped me get through this past year away from home and have supported me in all my endeavours. Finally, I'd like to thank my friends and coursemates from the M.Sc. - Aaron, Christoph, Jan, Jacques, Julian, Pranav, Michael and Vamsi, who've made this past year more than a little bearable.

Abstract

We aim to study the dynamics of spatially localised solutions in plane Couette flow. The solutions appear as "snakes" in the bifurcation diagram of the system and are conjectured to arise from the phenomenon of *homoclinic snaking*, which has been observed in lower dimensional pattern forming differential equations like the Swift–Hohenberg equation [1] and the subcritical complex Ginzburg–Landau equation [2].

These solutions are obtained by continuation of the localised edge state observed by Schneider *et al.* [3, 4] and Duguet *et al.* [5]. These edge states attract the minimal energy perturbations from the laminar profile and are self-sustained fixed points of the equations. They are critical in the transition to turbulence of wall-bounded shear flows like pipe and Couette flow where the laminar profile is linearly stable.

By time integrating these localised solutions over a range of Re, we show that there is no fixed transition Re. Instead, there is a range of Re in which most of the trajectories relaminarize interspersed with "windows", that provide routes to domain-filling chaos. Followed by this, there is a range of Re, in which most of the trajectories transition to domain-filling chaos interspersed with a few trajectories that relaminarize. Further, we investigate the dynamics of the fronts of the localised solutions at higher Re and show that the front motion is stochastic.

Table of Contents

List of Figures

List of Tables

1 Introduction

In plane Couette flow the coexistence of the linearly stable laminar state [6] along with turbulent dynamics suggests that there is a threshold, in perturbation amplitude, Reynolds number and in some way, shape (direction in phase space), that must be crossed for turbulence to be obtained [4]. This threshold forms a boundary in phase space (separatrix) between the laminar and turbulent dynamics, commonly referred to as the *edge of chaos* [7]. The entire edge is made, locally, by the stable manifolds of some invariant self-sustaining solutions called edge states [4]. Numerical studies by Schneider *et al.* [4], have shown that in wide and short domains at $Re \simeq 400$ one such edge state is a localised travelling wave solution of the Navier–Stokes equations. However, in wide and long domains at the same Re, the same studies have shown that, the edge state is a doubly localised structure which has internal chaotic dynamics (spatio-temporal chaos). In this case the edge state is not a fixed point or a periodic orbit but a turbulent spot. The significance of this edge state in terms of transition to turbulence lies in the fact that it evolves from the minimal energy perturbations that can exist away from the laminar solution, i.e., it is a fixed point/periodic orbit/chaotic attractor on the separatrix between the laminar and turbulent state. Its stable manifold is of co-dimension one [4] which emphasizes the fact that smaller perturbations will decay to the laminar state while larger ones will grow to turbulence. Also, in such large domains, the size of the edge state pattern is close to the minimum spot size for front propagation at uniform velocity as observed in [4] and discussed in [8].

Further work in [4] showed how the internally chaotic edge state in wide and long domains transitioned to turbulence/domain-filling chaos. Initially, there was in increase in the energy density with no change in localisation. Only once the energy within the spot increased to the turbulence level, did the spot start growing and filling the rest of the domain. In order to understand how transition actually occurs, we need to understand the dynamics of the fronts of these localised structures (edge states).

Later work by Schneider, Gibson and Burke [9], showed, by continuation of the edge state found in [4] that there are a multiplicity of localised structures in plane Couette flow. These states appear as snake-like branches on the bifurcation diagram of the system and bear striking similarity to localised states in some lower-dimensional systems (e.g. Swift–Hohenberg equation). Each point on the snake corresponds to a homoclinic orbit in space. By studying the dynamics of these localised solutions on larger domains and characterizing their growth and decay, we aim to contribute to the dynamical systems framework of transitional turbulence in shear flows.

In this chapter, we first discuss a similar phenomenon observed in the Swift–Hohenberg equation. Further, we discuss the dynamical features of the localised solutions in plane Couette flow found and described in [9]. The next chapter provides a description of the main numerical methods we used in our study. Followed by this, is a chapter detailing the major results we obtained. We conclude with a chapter discussing the main results and presenting the conclusions of our study.

1.1 The Swift–Hohenberg Equation

As mentioned earlier, a similar localisation phenomenon is observed in other systems, such as the one-dimensional Swift–Hohenberg equation. The system takes the form,

$$\frac{\partial u}{\partial t} = ru - (\partial_x^2 + q_c^2)^2 u + vu^2 - gu^3 = f(u) \tag{1-1}$$

where, $u = u(x,t)$. To observe the snaking phenomenon r is chosen as the parameter of the system while the other parameters are fixed at $v = 0.41$, $g = 1$ and $q_c = 0.5$ [1]. For periodic boundary conditions over a domain of length L, Equation (1-1) has a well-known Lyapunov functional given by

$$\mathcal{F}(u) = \int_0^L \left(-\frac{ru^2}{2} + \frac{1}{2}\left((\partial_x^2 + q_c^2)u\right)^2 - \frac{1}{3}vu^3 + \frac{1}{4}gu^4 \right) dx = -\int_0^L \int f(u) du dx \tag{1-2}$$

where, $\mathcal{F} : \mathbb{M} \to \mathbb{R}$ and $\frac{\partial u}{\partial t} = -\frac{\delta \mathcal{F}}{\delta u}$, where $\frac{\delta \mathcal{F}}{\delta u}$ is the Frechet derivative of $\mathcal{F}$ and $\mathbb{M}$ is the space of associated with the solutions u. We can thus say that,

$$\begin{aligned} \left(\frac{\partial u}{\partial t}\right)^2 &= -\frac{\delta \mathcal{F}}{\delta u}\frac{\partial u}{\partial t} \\ \implies \int_0^L \left(\frac{\partial u}{\partial t}\right)^2 dx &= -\int_0^L \frac{\delta \mathcal{F}}{\delta u}\frac{\partial u}{\partial t} dx \\ &= -\frac{\partial \mathcal{F}}{\partial t} \end{aligned} \tag{1-3}$$

Since the LHS of Equation (1-3) is either positive or zero, $\frac{\partial \mathcal{F}}{\partial t} < 0$ for $\frac{\partial u}{\partial t} \neq 0$ and $\frac{\partial \mathcal{F}}{\partial t} = 0$ for $\frac{\partial u}{\partial t} = 0$. This shows that any trajectory of the system reduces to a local minimum of $\mathcal{F}$ and also that the system cannot have any periodic orbits [10] and therefore no Hopf bifurcations are possible.

Burke and Knobloch [1] have shown that it is possible to obtain the spatially periodic solutions of the system by a numerical continuation algorithm. The solution branch obtained is the structural analogue of the Nagata solution (u_P) in plane Couette flow and is commonly referred to as the periodic branch [1]. Burke and Knobloch [1] have further shown that it is possible to construct localised solutions of Equation (1-1) that are biasymptotic to the trivial state $u = 0$. The time-independent system forms a dynamical system in space with 4 degrees of freedom i.e. $(u, u_x, u_{xx}, u_{xxx})$ [11] and it is clear to see that such solutions represent homoclinic orbits in the phase space of the system. The biasymptotic behaviour of the localised solutions requires the trivial states to have both stable and unstable directions (spatially). This is possible at values of $r < 0$, at which the trivial state has 2 stable and 2 unstable directions. To show this, we consider the linear stability analysis of the time-independent Swift–Hohenberg equation about the trivial state $u_0 = 0$,

$$ru - (\partial_x^2 + q_c^2)^2 u + vu^2 - gu^3 = 0 \tag{1-4}$$

We insert the Fourier mode perturbation, $\tilde{u} = \hat{u}e^{ikx}$ into the above equation and linearize it about u_0,

$$r\hat{u}e^{ikx} - (k^4\hat{u}e^{ikx} - 2q_c^2k^2\hat{u}e^{ikx} + q_c^4\hat{u}e^{ikx}) = 0 \tag{1-5}$$

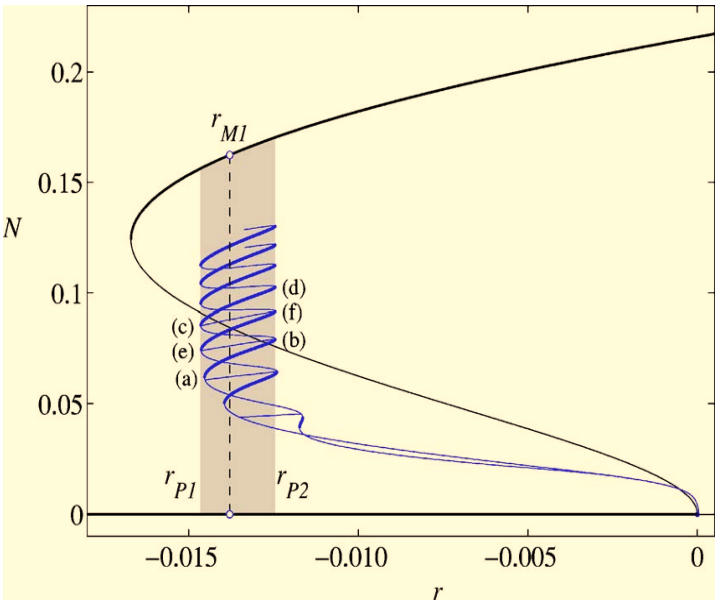

Figure 1-1: Homoclinic snaking in the one-dimensional Swift–Hohenberg equation, after Burke and Knobloch [1]. The lines in bold indicate stable solutions.

For which we get the fourth-order dispersion relation,

$$r - k^4 + 2q_c^2 k^2 - q_c^4 = 0 \tag{1-6}$$

We can solve this to get,

$$k = \pm\sqrt{q_c^2 \pm \sqrt{r}} \tag{1-7}$$

If we linearise k about $\sqrt{r} = 0$, we get,

$$ik = \pm iq_c \pm \sqrt{-r}/2q_c + \mathcal{O}(r) \text{ for } r < 0 \tag{1-8}$$

$$ik = \pm iq_c \pm i\sqrt{r}/2q_c + \mathcal{O}(r) \text{ for } r > 0 \tag{1-9}$$

We define $s = ik$ to represent an eigenvalue of the system. Thus for $r < 0$, we have four eigenvalues, 2 unstable and 2 stable. For $r > 0$, all the eigenvalues lie on the imaginary axis, so the fixed point is not hyperbolic. The same holds for $r = 0$, for which there exist two pairs of repeated eigenvalues on the imaginary axis. It is clear then that it is not possible to approach the trivial state $u_0 = 0$, once $r > 0$, so biasymptotic solutions cannot exist. Therefore, we cannot have localised solutions of the system for $r > 0$.

For values of $(r < 0, |r| \ll 1)$, two localised states have been found by using perturbation methods [1]. They take the form,

$$u_l(x) = 2\left(\frac{-2r}{\gamma_3}\right)^{\frac{1}{2}} \operatorname{sech}(x\sqrt{-r}/2q_c)\cos(q_c x + \phi) + \mathcal{O}(r) \tag{1-10}$$

As shown in [1], if all order terms are included in the asymptotics, the system selects 2 values of ϕ, i.e. $0, \pi$ and sets up a flow such that one of the solutions weakly repelling and the other is weakly attracting. The value of ϕ determines the phase of the localised pattern within the sech envelope.

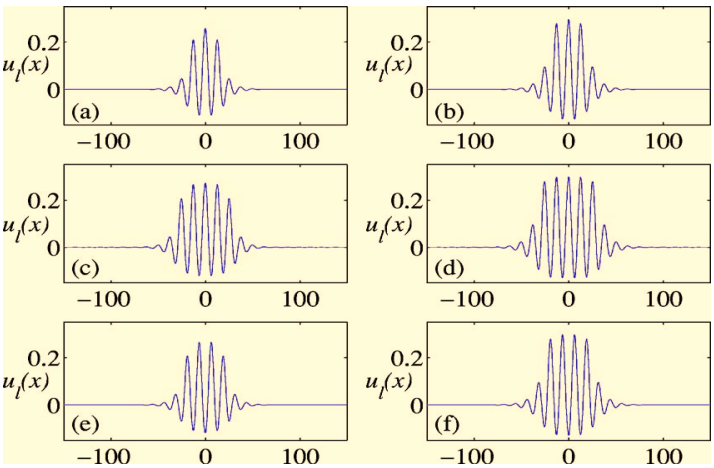

Figure 1-2: Localised solutions in the Swift–Hohenberg equation, after Burke and Knobloch [9]. The solutions (a)–(f) correspond to the same points in Figure 1-1.

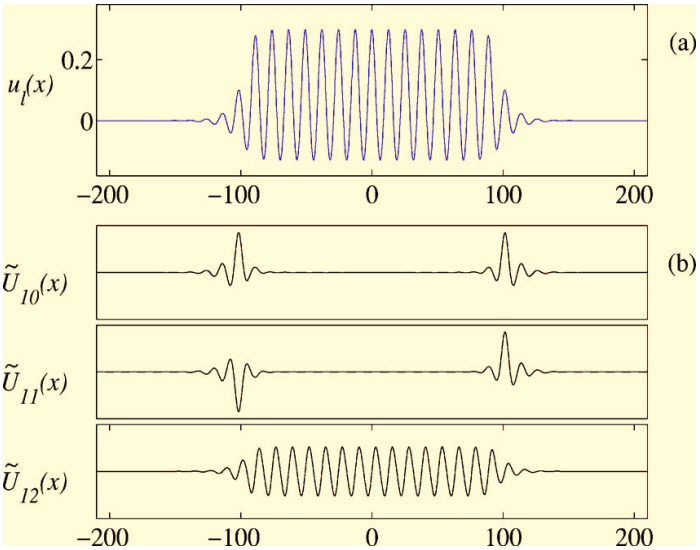

Figure 1-3: Eigenvectors of interest on the Swift–Hohenberg snake, after Burke and Knobloch [1].

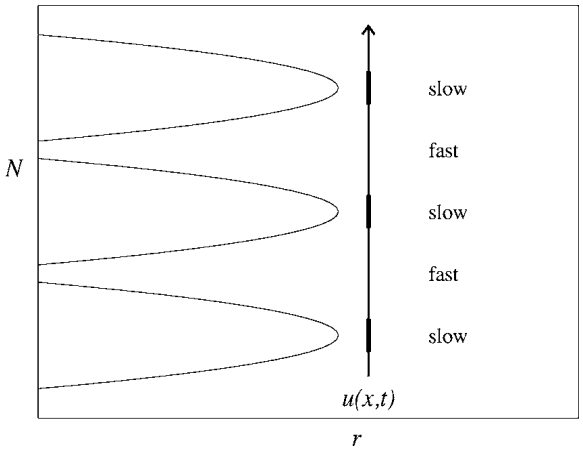

Figure 1-4: Depinning transition from the right saddle-nodes in the Swift–Hohenberg equation, after Burke and Knobloch [1], where N represents the L^2-norm of the fixed-point solutions u of Equation (1-1), i.e., $N^2 = \int_\Omega u^2 dx$ and r is the parameter as defined previously.

Further, by using numerical continuation, Burke and Knobloch [1] have also shown that these localised solutions extend far away from $r = 0$ in the direction of increasing $-r$ as can be seen in Figure 1-1. The snake-like structure of the branches of solutions is similar to the snaking seen in Couette flow. The point r_{M1} corresponds to a Maxwell point where the free energy $\mathcal{F}$ of the patterned branch (shown in bold) and the flat state have the same value. This indicates that if a front is placed between the two solutions [12], we may find another minimum of $\mathcal{F}$ (an equilibrium solution). Interestingly, even for values of r, in a small neighbourhood of r_{M1} called the "pinning" region equilibrium solutions are found. In this region even though the trivial state and the periodic branch have different values of $\mathcal{F}$, due to the structural stability of the snake [13] we can still find equilibrium solutions by placing a front between the two. A more detailed explanation of the snaking phenomenology based on the qualitative theory of differential equations can be found in [14, 13, 15].

The points r_{P1}, r_{P2} correspond to the boundaries of the pinning region away from the origin. It can be seen that the location of the saddle-node bifurcations on both sides of the snake asymptotes to these values of r. As the branches snake up localised nucleation occurs at the fronts as they pass through a series of saddle-node bifurcations. The structure of the solutions at various positions on the branch can be seen in Figure 1-2. A key difference between this phenomenon and that observed in plane Couette flow is that the upper branch of the patterned/periodic state is stable in this section of the parameter space, while in Couette flow the spatially periodic Nagata solution is unstable in the vicinity of the snake. The stability of the branches of the snake ($\phi = 0$ or π) alternates between stable and twice unstable. For the twice unstable branches the form of the eigenvectors is shown in Figure 1-3. The eigenvector $\tilde{U}_{10}$ corresponds to the nucleation/denucleation mode, while $\tilde{U}_{11}$ corresponds to the phase shift/symmetry breaking mode. Both of these are have positive growth rates on the unstable branches. $\tilde{U}_{12}$ has a zero growth rate everywhere on the snake and results from the translation invariance of the system. The rung branch between the two snakes originates from a symmetry-breaking bifurcation from either of the snakes. For a more detailed discussion of the branch stability and growth rates see [1].

Another significant aspect of the dynamics of these localised solutions is how they behave if perturbed in parameter space. This mechanism is often referred to as *depinning* [1]. If the solution is perturbed within the linear regime to lie outside to the left of r_{P1} it decays to the flat state while if it is perturbed

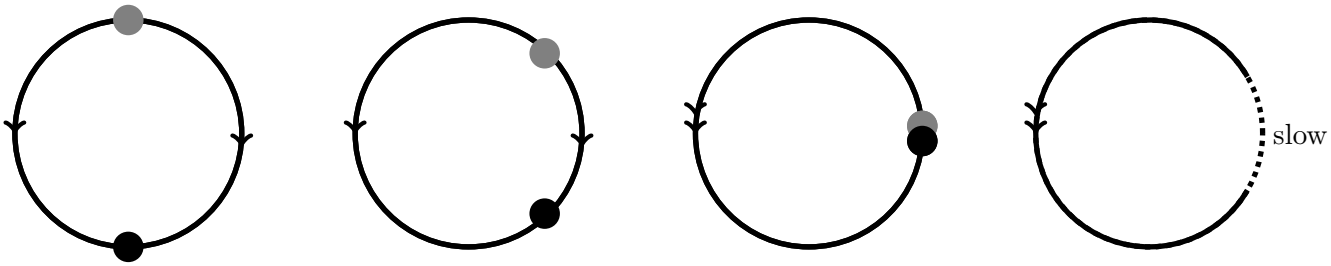

Figure 1-5: Alternating slow-fast dynamics associated with depinning. Moving from the middle of the pinning region towards the right saddle-nodes, it can be seen that as the unstable fixed point (grey) and the stable fixed point (black) get closer, the dynamics between the two fixed points becomes exponentially slow in one direction (towards the lower stable point) and exponentially fast in the other direction (towards the upper stable point), both of which are dynamically equivalent and can be represented by one point. Just to the right of the saddle-node the two annihilate each other but the characteristic slow-fast dynamics of the fixed points subsists. The dynamics in this section of parameter space are characteristic of a "SNIPER" bifurcation.

to lie to the right of r_{P2} it grows till the patterned state fills the entire domain. Due to the proximity to the saddle-node growth occurs in bursts.

Initially, the size of the pattern grows/decays slowly, followed by a rapid transition to the neighbourhood of the next saddle-node which is followed by a slow period of growth again. Thus growth (or decay) of the localised state occurs in intermittent bursts followed periods of asymptotically slow growth in the local neighbourhood of the saddle-node a shown in Figure 1-4. The mode responsible for growth in the linear regime is nearly identical to the localised nucleation mode of the nearest negative slope branch, which is one of its 2 unstable modes (the other being the symmetry breaking mode responsible for bifurcations of the rung states [1]). This process continues till the entire domain is filled by the spatially periodic solution [1]. The slow dynamics in the proximity of the saddle-node can be explained as follows. If all the positive slope branches of the snake are considered to be dynamically equivalent (a symmetry of sorts), they can be reduced to a single point on a given trajectory of the phase space. The same applies for all the negative slope branches which all have two unstable directions. At any fixed value of the parameter in the pinning region, perturbing the solution on the negative branch can thus be represented by the trajectory between a relative saddle (unstable) and a relative node (stable) as shown in Figure 1-5. While moving right from the centre of the pinning region, the two approach each and finally annihilate each other. However, the slow fast dynamics, characteristic of the two fixed points, subsists even slightly right of the saddle-nodes in parameter space. We aim to investigate whether a similar depinning mechanism is observed in the richer and more intricate dynamics of the full non-linear Navier–Stokes equations. A similar mechanism in the Navier–Stokes equations could provide a route to chaos.

1.2 Localised Solutions in Plane Couette Flow

Couette flow is the generic term used to represent a flow between two parallel walls moving in opposite directions, with zero pressure gradient (or a flow which is Gallilean invariant from such a flow). The non-dimensional height of the domain is equal to 2, such that the domain $\Omega \rightarrow (L_x, L_y, L_z) = (L_x, 2, L_z)$. The non-dimensional wall velocities are equal to ± 1 at the upper and lower walls respectively. The system being considered is represented by the non-dimensional incompressible Navier–Stokes equations, with no-slip boundary conditions at the upper and lower walls and periodic boundary

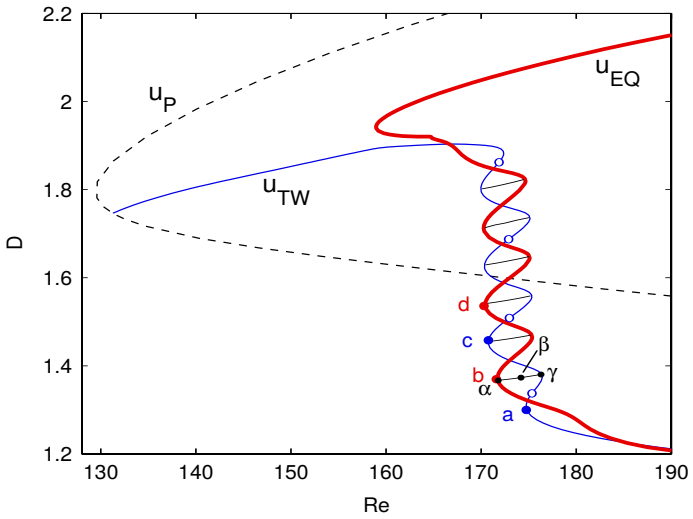

Figure 1-6: Homoclinic snaking in plane Couette flow, after Schneider *et al.* [9]. The blue branch u_{TW} is the travelling wave solution while the red branch u_{EQ} represents the equilibrium solution. The dashed branch u_P represents the spatially periodic Nagata solution [16].

conditions in the streamwise and spanwise directions, which are written as

$$\frac{\partial \mathbf{u}}{\partial t} + (\mathbf{u}.\nabla)\mathbf{u} = -\nabla p + \frac{1}{Re}\nabla^2 \mathbf{u}, \tag{1-11}$$

along with the continuity equation (to ensure incompressibility)

$$\nabla.\mathbf{u} = 0, \tag{1-12}$$

with boundary conditions at the top and bottom walls as

$$\mathbf{u}(x, y = \pm 1, z) = \pm 1, \tag{1-13}$$

and periodic boundary conditions at the other boundaries given by

$$\mathbf{u}(x = 0, y, z) = \mathbf{u}, (x = L_x, y, z), \tag{1-14}$$

$$\mathbf{u}(x, y, z = 0) = \mathbf{u}(x, y, z = L_z), \tag{1-15}$$

where $\mathbf{u}$ is the vectorial representation of the three-dimensional velocity field, ∇p is the pressure gradient, which for Couette flow is zero and $Re = \frac{Uh}{\nu}$ is the Reynolds number, with U as half the difference between the wall velocities, h as half the channel height, and ν as the kinematic viscosity of the fluid. It is trivial to see that the laminar solution of this system, $\mathbf{U}$ is given by

$$\mathbf{U}.\hat{\mathbf{i}} = y, \tag{1-16}$$

$$\mathbf{U}.\hat{\mathbf{j}} = 0, \tag{1-17}$$

$$\mathbf{U}.\hat{\mathbf{k}} = 0, \tag{1-18}$$

where $\hat{\mathbf{i}}$, $\hat{\mathbf{j}}$, and $\hat{\mathbf{k}}$ represent the unit vectors in the x, y and z directions respectively. This laminar solution represents a fixed point of the system, i.e., $\frac{\partial \mathbf{U}}{\partial t} = 0$. It can be used to decompose any solution

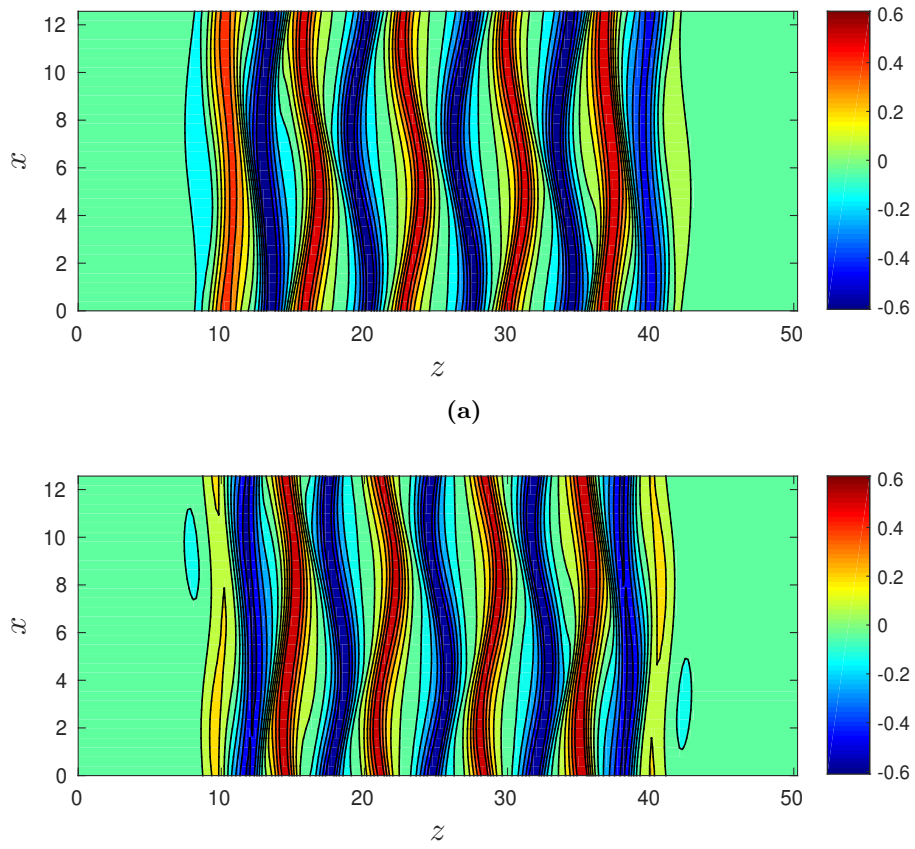

Figure 1-7: Midplane contour plots of $\mathrm{u_{EQ}}$ (a) and $\mathrm{u_{TW}}$ (b). Contours are coloured by the value of the streamwise non-laminar velocity u. Solutions for a domain size of $4\pi \times 2 \times 16\pi$, provided by John F. Gibson.

into two parts

$$\mathbf{u} = \mathbf{U} + \boldsymbol{u} \tag{1-19}$$

where $\boldsymbol{u}$ is the fluctuation (not necessarily in the linear regime) to the laminar solution, with u, v, w the streamwise (x), wall-normal (y) and spanwise (z) components of $\boldsymbol{u}$ respectively.

Work in [9] has demonstrated that continua of localised solutions of plane Couette flow can be obtained by continuation of the edge state solution at $Re = 400$ for domain sizes of $4\pi \times 2 \times 8\pi$ and $4\pi \times 2 \times 16\pi$. The solutions were found to exhibit the phenomenon of *homoclinic snaking* as seen in the bifurcation diagram in Figure 1-6. These localised solutions occur in a "pinning" region of the parameter space of the system, where the parameter is the Reynolds number Re, as previously defined. The quantity D in the figure is the dissipation per unit volume of the entire velocity field, written as $D = (1/V) \times \int_\Omega (|\nabla \times \mathbf{u}|^2) d\Omega$, with $V = L_x \times L_y \times L_z$ the volume of the domain Ω, and is just a measure used to represent the solutions on the bifurcation diagram. Another quantity that will be useful later is the dissipation per unit volume of the fluctuation field, $d = (1/V) \times \int_\Omega (|\nabla \times \boldsymbol{u}|^2) d\Omega$.

There are two branches of the snake, both representing localised solutions. The blue one represents travelling wave solutions, while the red one represents fixed point equilibria of the system. The solutions on the $\mathrm{u_{EQ}}$ branch have the reflection symmetry $\mathcal{R}$, $[u, v, w](x, y, z, t) \to [-u, -v, -w](-x, -y, -z, t)$, while those on the $\mathrm{u_{TW}}$ branch have shift-reflect symmetry $\mathcal{S}$, $[u, v, w](x, y, z, t) \to [u, v, -w](x + L_x/2, y, -z, t)$. The generic structure of the solutions is shown in the contour plots in Figure 1-7.

The travelling wave solutions also satisfy $[u, v, w](x, y, z, t) \to [u, v, w](x - ct, y, z, 0)$ where c is the streamwise phase velocity of the solution. It is interesting to note that all the symmetries above are also symmetries of the system (the Navier–Stokes equations in the plane Couette configuration). As a consequence of this, we can apply each of these symmetries to any solution that doesn't have them and generate new velocity fields which are necessarily solutions of the system.

It is also demonstrated in [9] that as Re is decreased the branches of localised solutions i.e. the snakes, climb up in the value of their dissipation and undergo numerous sub- and super-critical saddle-node bifurcations which nucleate rolls at the front of the localised solutions while preserving symmetry.

The snakes also show a series rung solutions, between the branches, in the proximity of the saddle-nodes [9]. The solutions on the rungs are travelling wave solutions themselves and form a smooth interpolation between the symmetry subspaces of the $\mathcal{S}$-symmetric travelling wave and the $\mathcal{R}$-symmetric equilibrium solutions [9].

Apart from the snake and the rungs, the dashed line indicates the spatially periodic Nagata solution [16]. As the snake keeps moving upwards in dissipation it eventually splits up as $\mathrm{u_{TW}}$ joins $\mathrm{u_P}$ while at least for this domain size $\mathrm{u_{EQ}}$ does not join any branch till at least $Re = 300$ [9]. The localised structures are formed due to pinning of fronts to the Nagata solution, i.e., the solution goes from the stable laminar state to the periodic solution and then back to the stable laminar state forming a homoclinic orbit (the system is treated as a dynamical system in space). Thus each point on the snake is such a homoclinic orbit in phase space and thus the term *"homoclinic snaking"*.

2 Methods

2.1 Time Integration - Direct Numerical Simulation

Whenever time integration routines were required, they were carried out using the direct numerical simulation subroutine of `Channelflow` [17], a spectral Navier–Stokes solver for both plane Poiseulle and plane Couette flow written in `C++`. The `couette` program was modified as required to perform specialised operations. The features of the solver are described below.

2.1.1 Discretization

Since the solution to the equations is sought in spectral space, the solution is discretized with Fourier, Chebyshev and Fourier points in the x (streamwise), y (wall-normal) and z (spanwise) directions respectively. The Fourier points, which are uniformly spaced, lend themselves conveniently to the periodic boundary conditions in the x and z directions, while the Chebyshev (extrema) points in the y direction are automatically refined near the walls. In general, a three-dimensional flowfield is represented as,

$$\mathbf{u}(\mathbf{x}) = \sum_{k_x=-\frac{N_x}{2}+1}^{N_x} \sum_{n_y=0}^{N_y-1} \sum_{k_z=-\frac{N_z}{2}+1}^{N_z} \hat{\hat{\mathbf{u}}}_{k_x,n_y,k_z} T_{n_y} e^{2\pi i(k_x x/L_x + k_z z/L_z)}, \tag{2-1}$$

where k_x and k_z are the wavenumbers in the x and z directions respectively, N_x, N_y, N_y are the number of points in the x, y, z directions respectively, T_m is the m^{th} Chebyshev polynomial of the first kind on the domain $[-1, 1]$ and $\hat{\hat{\mathbf{u}}}$ represents a third rank tensor of the spectral coefficients arising from a combined Fourier transform in the $x - z$ direction and a Chebyshev transform in the y direction. For our study we have used, 32 points in the x direction, 512 points in the z direction and 33 points in the y direction.

2.1.2 Base Flow-Fluctuation Decomposition

`Channelflow`, by default, decomposes the velocity field $\mathbf{u}$ and the pressure field p into a base and fluctuating part as follows,

$$\mathbf{u} = U(y)\hat{\mathbf{i}} + \boldsymbol{u}(\mathbf{x}, t), \tag{2-2}$$

$$\mathrm{p} = \Pi(t)x + p(\mathbf{x}, t), \tag{2-3}$$

where the velocity field is decomposed into a time-independent y-dependent base flow $U(y)$ and a fluctuating vector field $\boldsymbol{u}(\mathbf{x}, t)$ and the pressure field is decomposed into a linear in x time dependent base field $\Pi(t)x$ and fluctuation field $p(\mathbf{x}, t)$. This generalised decomposition makes it compatible with both plane Couette and plane Poiseulle base flows. For our case of plane Couette flow, we have,

$$U(y) = y, \tag{2-4}$$

$$\Pi(t) = 0. \tag{2-5}$$

If plugged into the Navier–Stokes (for the Couette flow configuration) the system is reduced to,

$$\frac{\partial \boldsymbol{u}}{\partial t} + \nabla p = \frac{1}{Re}\nabla^2 \boldsymbol{u} - (\boldsymbol{u}.\nabla)\boldsymbol{u} - y\frac{\partial \boldsymbol{u}}{\partial x} - v\hat{\mathbf{i}}, \tag{2-6}$$

$$\nabla \cdot \boldsymbol{u} = 0. \tag{2-7}$$

2.1.3 Treatment of Nonlinearity

The DNSFlags object also provides various options of manners in which to treat the non-linear advective term of the Navier-Stokes. The options available are,

- Convective form : $\mathbf{u}.\nabla\mathbf{u}$
- Divergence form : $\nabla.(\mathbf{uu})$
- Skew Symmetric form : $\frac{1}{2}\mathbf{u}.\nabla\mathbf{u} + \frac{1}{2}\nabla.(\mathbf{uu})$
- Rotational form : $(\nabla \times \mathbf{u}) \times \mathbf{u} + \frac{1}{2}\nabla.(\mathbf{uu})$

The above forms are exactly the same in continuous mathematics as long as the $\nabla.\mathbf{u} = 0$ is satisfied. In discretized mathematics, they are not all the same, in terms of both accuracy and computational efficiency. As mentioned in the channelflow documentation, the rotational form is the cheapest, although it has problems correctly resolving high spatial frequencies. The skew-symmetric form is about twice as expensive to compute, although it shows no such errors. The errors in the rotational form can be removed by using de-aliased transforms in the $x-z$ direction which is the default approach for dealing with the non-linearity and which is the method we have used for our investigation. Another possibility is the use of an alternating form of the non-linearity which alternates between the convective and divergence forms every timestep so as to reduce the computational cost associated with the skew-symmetric form.

`Channelflow` first decomposes the nonlinear term into the base flow and fluctuation and then computes $\boldsymbol{u} \cdot \nabla \boldsymbol{u}$ using the rotational form,

$$\mathbf{u} \cdot \nabla \mathbf{u} = (\nabla \times \boldsymbol{u}) \times \boldsymbol{u} + U\frac{\partial \boldsymbol{u}}{\partial x} + v\frac{\partial U}{\partial y}\hat{\mathbf{i}} + \frac{1}{2}\nabla(\boldsymbol{u} \cdot \boldsymbol{u}). \tag{2-8}$$

Inserted into Equation (2-6) for the plane Couette system ($U(y) = y$), this becomes,

$$\frac{\partial \boldsymbol{u}}{\partial t} + \nabla(p + \frac{1}{2}\nabla(\boldsymbol{u} \cdot \boldsymbol{u})) = \frac{1}{Re}\nabla^2 \boldsymbol{u} - ((\nabla \times \boldsymbol{u}) \times \boldsymbol{u} + y\frac{\partial \boldsymbol{u}}{\partial x} + v\hat{\mathbf{i}}). \tag{2-9}$$

To simplify Equation (2-9) we can write it as

$$\frac{\partial \boldsymbol{u}}{\partial t} + \nabla(q) = \mathbf{L}\boldsymbol{u} - \mathbf{N}(\boldsymbol{u}), \tag{2-10}$$

where

$$q = p + \frac{1}{2}\nabla(\boldsymbol{u} \cdot \boldsymbol{u}), \tag{2-11}$$

is a modified pressure term,

$$\mathbf{L} = \frac{1}{Re}\nabla^2, \tag{2-12}$$

is a linear operator, and

$$\mathbf{N}(\boldsymbol{u}) = ((\nabla \times \boldsymbol{u}) \times \boldsymbol{u} + y\frac{\partial \boldsymbol{u}}{\partial x} + v\hat{\mathbf{i}}), \tag{2-13}$$

is a nonlinear operator. The next step is to take a continuous Fourier tranform in the $x - z$ direction, which gives us,

$$\frac{\partial \tilde{\boldsymbol{u}}}{\partial t} + \tilde{\nabla}(\tilde{q}) = \tilde{\mathbf{L}}\tilde{\boldsymbol{u}} - \widetilde{\mathbf{N}(\boldsymbol{u})}, \tag{2-14}$$

where $\tilde{\boldsymbol{u}}$ and $\tilde{q}$ are the Fourier transforms of $\boldsymbol{u}$ and q respectively, and $\tilde{\nabla}, \tilde{\mathbf{L}}$ are the Fourier transforms of the operators ∇ and $\mathbf{L}$.

2.1.4 Time-stepping

`Channelflow` offers two main time-stepping schemes - a mixed Crank–Nicholson/Adams–Bashforth scheme and a mixed 3rd order Runge–Kutta scheme. As mentioned in the documentation, both schemes treat the linear term implicitly and the non-linear term explicitly. For this investigation, we have used exclusively the former. Let $\tilde{\boldsymbol{u}}^n$ be the approximation of $\tilde{\boldsymbol{u}}$ at the time $T = n\Delta t$, where Δt is the timestep. The mixed Crank—Nicholson/Adams–Bashforth second order scheme works by approximating the terms in Equation (2-14) at $T = (n + 1/2)\Delta t$ as follows,

$$\frac{\partial \tilde{\boldsymbol{u}}}{\partial t}^{n+1/2} = \frac{\tilde{\boldsymbol{u}}^{n+1} - \tilde{\boldsymbol{u}}^n}{\Delta t} + \mathcal{O}(\Delta t^2), \tag{2-15}$$

$$\tilde{\mathbf{L}}\tilde{\boldsymbol{u}}^{n+1/2} = \frac{1}{2}\tilde{\mathbf{L}}\tilde{\boldsymbol{u}}^{n+1} + \frac{1}{2}\tilde{\mathbf{L}}\tilde{\boldsymbol{u}}^n + \mathcal{O}(\Delta t^2), \tag{2-16}$$

$$\tilde{\nabla}\tilde{q}^{n+1/2} = \frac{1}{2}\tilde{\nabla}\tilde{q}^{n+1} + \frac{1}{2}\tilde{\nabla}\tilde{q}^n + \mathcal{O}(\Delta t^2), \tag{2-17}$$

$$\tilde{\mathbf{N}}^{n+1/2} = \frac{3}{2}\tilde{\mathbf{N}}^n - \frac{1}{2}\tilde{\mathbf{N}}^{n-1} + \mathcal{O}(\Delta t^2), \tag{2-18}$$

where $\tilde{\mathbf{N}}^n = \widetilde{\mathbf{N}(\boldsymbol{u}^n)}$. The way the linear term is approximated is called the Crank–Nicholson method and the way the nonlinear term is approximated is called the Adams–Bashforth method. Essentially, the Adams–Bashforth method tries to deal with nonlinear terms pseudo-explicitly by extrapolating a linear curve between $\tilde{\mathbf{N}}^{n-1}$ and $\tilde{\mathbf{N}}^n$ to $\tilde{\mathbf{N}}^{n+1}$,

$$\begin{aligned}
\tilde{\mathbf{N}}^{n+1/2} &= \frac{1}{2}\tilde{\mathbf{N}}^{n+1} + \frac{1}{2}\tilde{\mathbf{N}}^n \\
&= \frac{1}{2}\left(\frac{\tilde{\mathbf{N}}^n - \tilde{\mathbf{N}}^{n-1}}{\Delta t}2\Delta t + \tilde{\mathbf{N}}^{n-1}\right) + \frac{1}{2}\tilde{\mathbf{N}}^n \\
&= \frac{3}{2}\tilde{\mathbf{N}}^n - \frac{1}{2}\tilde{\mathbf{N}}^{n-1}.
\end{aligned}$$

Finally, when we insert this into Equation (2-14) we get (dropping the $\mathcal{O}(\Delta t^2)$ terms),

$$\left(\frac{1}{\Delta t} - \tilde{\mathbf{L}}/2\right)\tilde{\boldsymbol{u}}^{n+1} + \frac{1}{2}\tilde{\nabla}\tilde{q}^{n+1} = \left(\frac{1}{\Delta t} + \tilde{\mathbf{L}}/2\right)\tilde{\boldsymbol{u}}^{n} - \frac{1}{2}\tilde{\nabla}\tilde{q}^{n+1} + \frac{3}{2}\tilde{\mathbf{N}}^{n} - \frac{1}{2}\tilde{\mathbf{N}}^{n-1}. \tag{2-19}$$

This option for timestepping needs to be passed as a variable of the DNSFlags object of the DNS class of solver. Apart from this, `Channelflow` also offers the option of fixed and variable time-stepping, fixed being the default. Variable time-stepping is done while keeping the time-step within a specified range, the CFL number below a certain value and the timestep as a whole number fraction of some time-interval so that the simulation can be stopped and the results observed. For more information on time-stepping, discretization and capabilities of `Channelflow`, the reader is invited to have a look at the documentation [17].

2.2 Continuation - Newton–Krylov Hookstep Algorithm

Numerical continuation of fixed points or periodic orbits of plane Couette flow, when required, was performed using the `continuesoln` program of `Channelflow` [17] which uses the Newton-Krylov iteration with a locally constrained hookstep [18] to find fixed points or periodic orbits given a good initial guess. Once found the solutions are then continued by pseudo arc-length extrapolation, which enables traversal of saddle-nodes and other topologically intricate structures of the systems bifurcation diagram. A brief description of a typical continuation algorithm is given below.

2.2.1 Problem Statement

For the sake of simplicity, we consider continuation of only fixed points/equilibria. Given a reasonably good initial guess, $\mathbf{u_g}$, the aim of continuation is to converge this guess and find an entire branch of solutions in parameter space which are fixed points, i.e., an entire family of fixed points $(\mathbf{u}, Re)$ parametrized by the Reynolds number such that,

$$f(\mathbf{u}, Re) = 0, \tag{2-20}$$

where f is the non-linear operator associated with the Navier–Stokes equations, i.e.,

$$f(\mathbf{u}, Re) = \frac{1}{Re}\nabla^2\mathbf{u} - \nabla p - (\mathbf{u}\cdot\nabla)\mathbf{u} \tag{2-21}$$

2.2.2 Newton Step

Since we have a good initial guess, $\mathbf{u_g}$ at a particular Re, which we assume lies in the linear regime, all we need to do is find the correction vector to this guess, i.e.,

$$f(\mathbf{u_g} + \delta\mathbf{u}) = 0, \tag{2-22}$$

$$f(\mathbf{u_g}) + \delta\mathbf{u}.\mathbf{D}_{\mathbf{u_g}} f + \mathcal{O}(\delta\mathbf{u}^2) = 0. \tag{2-23}$$

If we solve Equation (2-23) iteratively we will converge to a minimum of $f(\mathbf{u})$. At every step we correct as follows : $\mathbf{u_g} \leftarrow \mathbf{u_g} + \delta\mathbf{u}$. The convergence will be quadratic because the error in the equation is of order $\delta\mathbf{u}^2$.

2.2.3 Krylov Subspace Methods

Equation (2-23) when discretized is essentially a matrix-vector system. If we have N^3 points in our velocity field, the Jacobian $\mathbf{D_{u_g}} f$ will be $N^3 \times N^3$. Storage of such large matrices is impossible for fine meshes. So traditional matrix inverse methods like LU factorization, QR decomposition etc. cannot be used. Most continuation algorithms use some form of iterative subspace method to find the solution of the large matrix-vector systems like Equation (2-23). Commonly used methods are GMRES (Generalised Minimal Residual), which is used by `continuesoln` and the stabilised biconjugate gradient method.

2.2.4 Extrapolation

Once $\delta\mathbf{u}$ has been found to a reasonable tolerance, we add it to the initial guess $\mathbf{u_g}$ to get an initial fixed point $\mathbf{u_i} = \mathbf{u_g} + \delta\mathbf{u}$ for the continuation algorithm. To find the next fixed point we need to find the tangent vector to the point $(\mathbf{u_i}, Re_i)$. We can do this as follows:

$$f(\mathbf{u_i} + \delta\mathbf{u}, Re_i + \delta Re) = \cancelto{0}{f(\mathbf{u_i}, Re_i)} + \begin{pmatrix} \mathbf{D_{u_i}} & \mathbf{D_{Re_i}} \end{pmatrix} \begin{pmatrix} \delta\mathbf{u} \\ \delta Re \end{pmatrix} = 0 \tag{2-24}$$

The vector $\begin{pmatrix} \delta\mathbf{u} & \delta Re \end{pmatrix}$ is the tangent vector to the curve $(\mathbf{u}, Re)$ at $(\mathbf{u_i}, Re_i)$. We can now normalize this vector to get $(\mathbf{u_i}, Re_i)/||(\mathbf{u_i}, Re_i)|| = \hat{\mathbf{u_T}}$, the unit vector along this direction. We then add a small perturbation $\delta\mathbf{u_s} = \epsilon\hat{\mathbf{u_T}}$ to the field $(\mathbf{u_i}, Re_i)$ along the direction of this vector. The new perturbed field $(\mathbf{u}*, Re*)$ enters the Newton step as the new guess field $\mathbf{u_g}$. If converged we continue in the same manner, else we reduce the amount of the perturbation and retry. This method of continuation is referred to as pseudo-arclength extrapolation.

A less computationally intensive method [19] involves extrapolating 3 previous fixed solutions $(\mathbf{u_n}, Re_n)$, $(\mathbf{u_{n-1}}, Re_{n-1})$, $(\mathbf{u_{n-2}}, Re_{n-2})$ to get the new guess solution for $(\mathbf{u_{n+1}}, Re_{n+1})$, as this does not require computing the tangent vector at every step.

2.3 Resources

We used the local `Linux/AERO` compute clusters to carry out our computations. Most time integration routines require in excess of 16 cores to run at the maximum possible speed. The continuation only needed a single processor as the code is not vectorised.

For the entire study, about 1200 hours of wall computing time were used for time integration. In addition to this about 700 hours of wall computing time were used by the continuation algorithm.

3 Results

3.1 Low Reynolds Number Turbulence

Experimental studies by Dauchot and Daviaud [20] have shown that, for plane Couette flow, there exists a non-linear critical Reynolds number $Re_{NC} = 325 \pm 5$ below which finite-amplitude perturbations of any amplitude to the laminar profile are not sustained and decay back to the laminar state. Above Re_{NC}, for every Reynolds number, there exists a critical amplitude $A_C(Re)$ above which spatially and temporally localised perturbations expand and form spatially bounded turbulent spots (which are sustained for a long time in comparison to the growth time of the spot) and below which they decay back to the laminar state (or are sustained for a time of the same order as the growth time of the spot) [20]. Numerical studies by Shi *et al.* [21] have confirmed that there exist a critical Re in plane Couette flow for localised turbulent stripes to be sustained. They tested a range (300) of initial conditions (turbulent stripes) at Reynolds numbers $\in [310, 350]$ using the computational domain proposed by Tuckerman and Barkley [22] and observed whether the stripe split or decayed. Using the results, they were able to compute a mean splitting time and a mean decay time for each Re and thus obtain a critical Re where the two curves intersect. They observed that beyond this critical Re the spatial proliferation of the stripes outweighed the inherent decay (probably associated with an amplitude killing mode) and the spatially extended turbulence was sustained. The critical Reynolds number, $Re \simeq 325$, found by Shi *et al.* is remarkably close to that found experimentally by Dauchot and Daviaud.

These turbulent spots/stripes (along with other turbulent structures at lower Re) must however be distinguished from the conventional turbulent flows at higher Re in that they lack the range of spatial and temporal scales associated with the latter. Nonetheless, they are chaotic in nature. A Direct Numerical Simulation using `Channelflow` [17] at $Re = 400$ (well above Re_{NC}) for $T = 50$ units of time in a domain size of $4\pi \times 2 \times 16\pi$ exhibits the chaotic trajectories expected from this system. The initial condition is taken to be a random finite amplitude perturbation from the laminar profile. Using the L^2-norms of the non-laminar (fluctuation) u, v, w components of the velocity field as measures of the dynamical system, phase space diagrams can be obtained as seen in Figure 3-1. The independent time-evolution of the components can be seen in Figure 3-2. The chaotic nature of the trajectories is clearly visible.

Further evidence of the chaotic nature of system lies in its sensitivity to initial conditions. When the initial random field is perturbed within the linear regime and time-integrated the two trajectories, the initial field and the perturbed field, should diverge after some time if the system is chaotic. We perturbed the initial random field with a perturbation $\mathbf{u}^*$ of the form,

$$\mathbf{u}^*(\mathbf{x}) = \sum_{k_x=-\frac{N_x}{2}+1}^{N_x} \sum_{n_y=0}^{N_y-1} \sum_{k_z=-\frac{N_z}{2}+1}^{N_z} \hat{\tilde{\mathbf{a}}}_{k_x,n_y,k_z} T_{n_y} e^{2\pi i(k_x x/L_x + k_z z/L_z)} \tag{3-1}$$

where $\hat{\tilde{\mathbf{a}}}_{k_x,n_y,k_z} = \text{rand}[-1,1] s^{(|k_x|+|n_y|+|k_z|)}$ (rand represents `C++`'s default pseudo-random number generator), where s is a user defined parameter indicating the smoothness of the field.

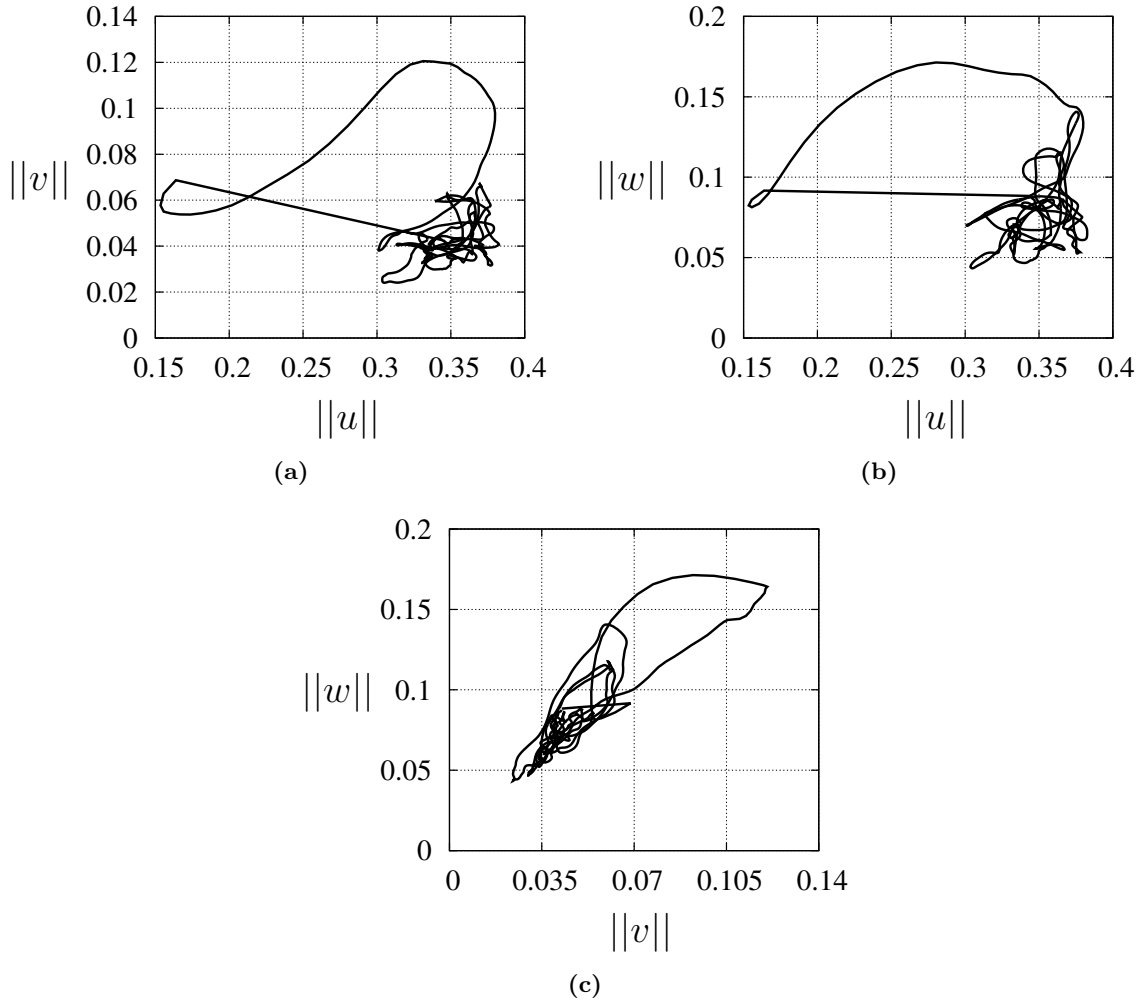

Figure 3-1: Chaotic trajectories representative of low Re turbulence represented by phase space plots of $||u||$ vs $||v||$ (a), $||u||$ vs $||w||$ (b), and $||v||$ vs $||w||$ (c), where u, v and w are the non-laminar streamwise, spanwise and wall-normal components of the fluctuation velocity field respectively, for a domain size $4\pi \times 2 \times 16\pi$ ($Re = 400$). The excursion observed in the plot represents the initial trajectory of the solution before it enters what appears to be the turbulent attractor.

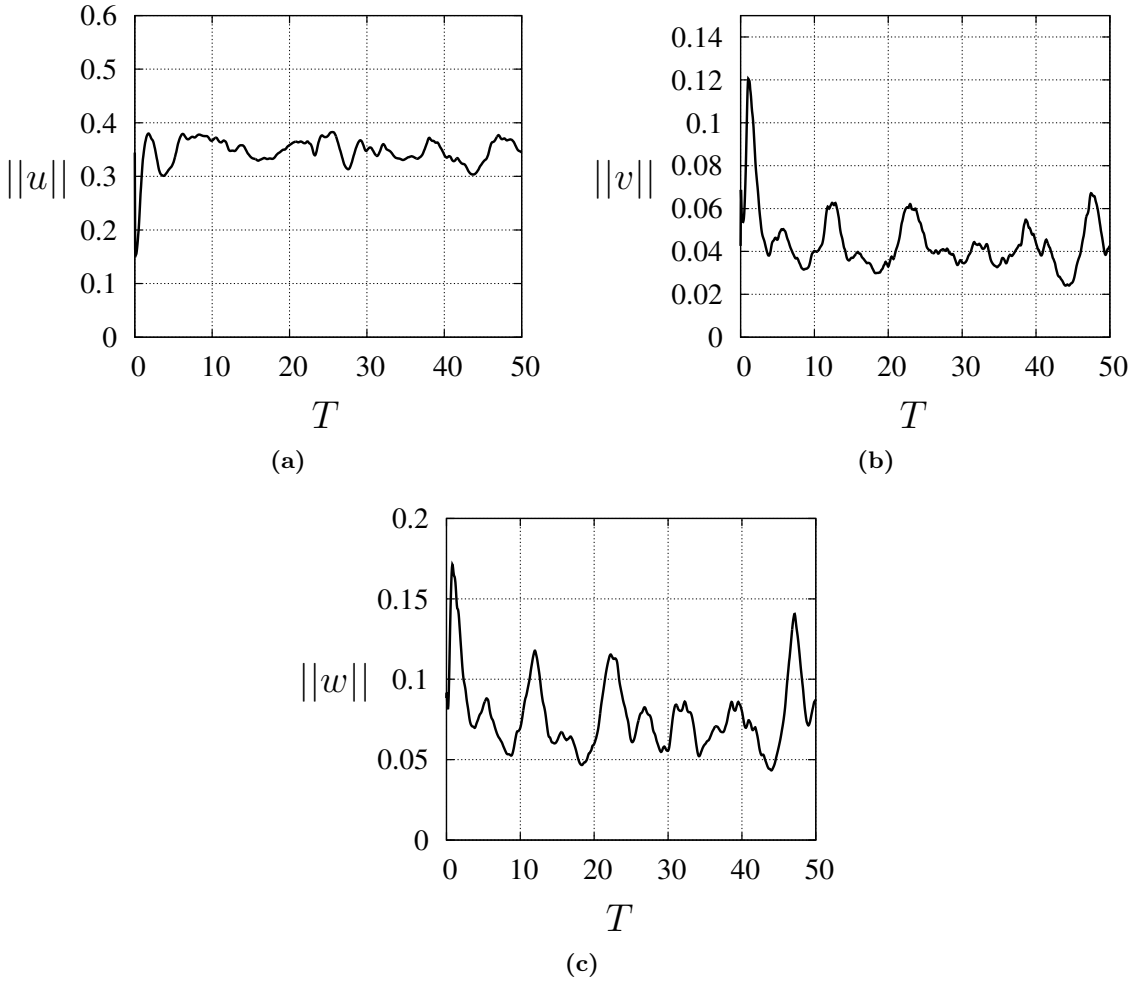

Figure 3-2: Time evolution of $||u||$ (a), $||v||$ (b), and $||w||$ (c), at $Re = 400$ for a random perturbation to the laminar profile.

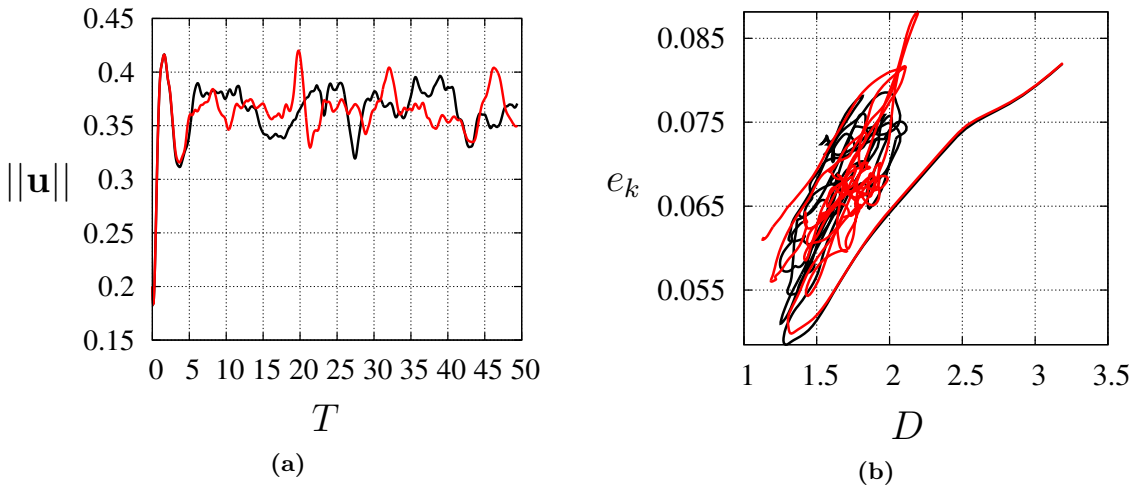

Figure 3-3: Sensitivity to initial conditions indicated by time evolution of the L^2-norms of the initial (black) and perturbed (red) solutions (a), and phase space plots of D (dissipation as defined previously) and non-laminar/fluctuation kinetic energy e_k (b).

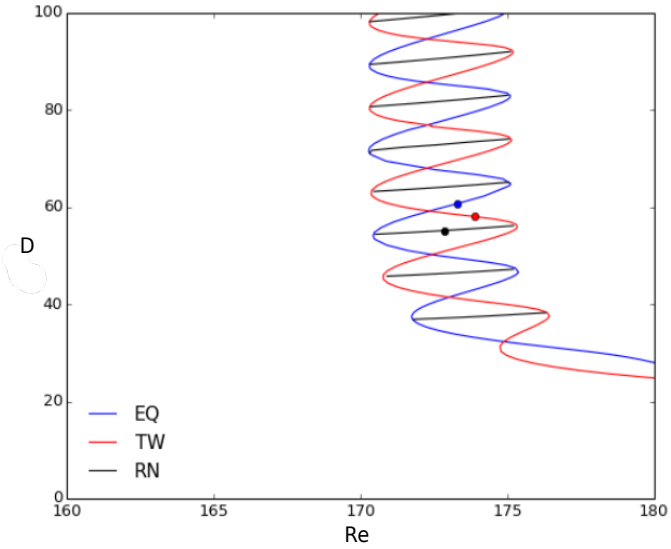

Figure 3-4: Initial solutions on snake in $4\pi \times 2 \times 16\pi$ domain provided by John F. Gibson. D and Re stand for the Dissipation and Reynolds number as defined earlier. **EQ** is the equilibrium solution branch, **TW** is the travelling wave branch and **RN** is the rung branch.

Solution	Re	D
Equilibrium	173.3108	1.60451
Travelling Wave	173.8691	1.57773
Rung	172.87	1.54913

Table 3-1: Reynolds number and dissipation of exact solutions for domain size $4\pi \times 2 \times 16\pi$. Solutions correspond to the points in bold on the bifurcation diagram in Figure 3-4.

Further, the field is rescaled by $m/(||\mathbf{u}^*||)$, m being another user-defined parameter. We have taken the values of s and m to be 0.4 and 10^{-4} respectively. Further corrections are made to make sure the field satisfies continuity and Dirichlet boundary conditions at the walls. The results of such a time integration can be seen in Figure 3-3. The initial and perturbed solutions start together and follow each other until they enter what appears to be the turbulent attractor after which they separate and diverge. This is visible both from the time evolution of the norms of the solution and the phase space plots which use the dissipation D of the entire field and the non-laminar (fluctuation) kinetic energy per unit volume (e_k or $k = \frac{1}{2V}\int_\Omega ||\boldsymbol{u}||^2 d\Omega$) as measures of the dynamical system.

3.2 Continuation

We were provided with three solutions on the snake for a domain size of $4\pi \times 2 \times 16\pi$ by John F. Gibson from the University of New Hampshire. Their approximate location on the bifurcation diagram can be seen in Figure 3-4. The values of the Reynolds number and dissipation of the three solutions is given in Table 3-1. In our study, we have only used the equilibrium solution.

Although we did perform some time integration on these smaller domain sizes ($4\pi \times 2 \times 16\pi$), we were more interested in the larger domain sizes (especially in the localisation direction) so that the effects of front propagation would be more visible and domain size effects would not kick in for quite some time. Keeping this in mind, we doubled the size of the domain in the z direction from 16π to 32π. Although possible, this was not done using numerical continuation, with L_z as the parameter, due

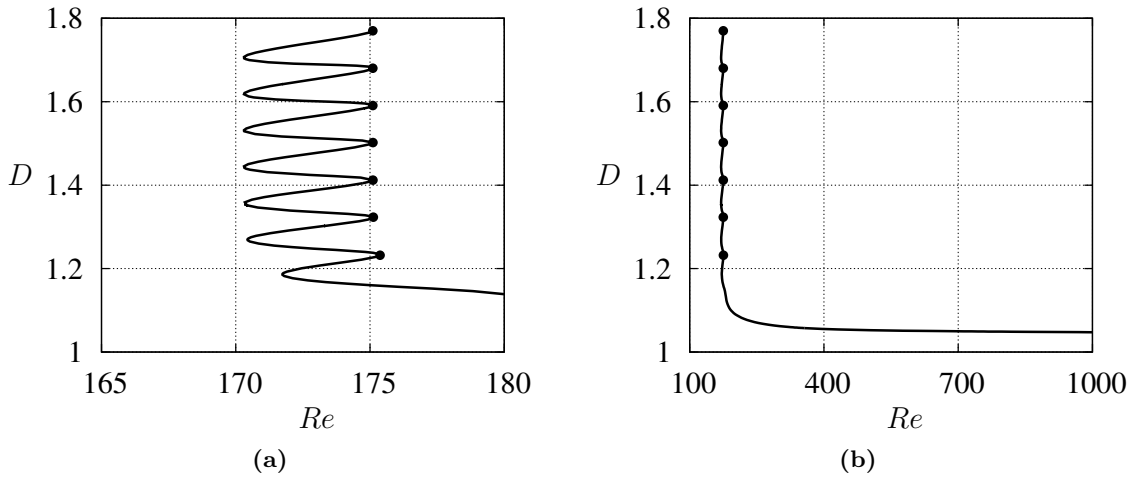

Figure 3-5: D vs. Re for the $4\pi \times 2 \times 32\pi$ domain - The snake in the large domain (a) and the snake along with other localised solutions upto $Re = 1000$ (b). The right-hand saddle-nodes on the snake are marked in bold.

Saddle-Node	Re	D
$\mathbf{S_0}$	175.37554	1.2320437
$\mathbf{S_1}$	175.12373	1.3230843
$\mathbf{S_2}$	175.10799	1.412104
$\mathbf{S_3}$	175.10993	1.5020502
$\mathbf{S_4}$	175.10458	1.5908167
$\mathbf{S_5}$	175.10613	1.6802624
$\mathbf{S_6}$	175.10417	1.7698695

Table 3-2: Reynolds number and dissipation of exact solutions at the right hand saddle-nodes for domain size $4\pi \times 2 \times 32\pi$. Solutions correspond to the points in bold on the bifurcation diagram in Figure 3-5, starting from the lowest saddle-node $\mathbf{S_0}$ to the highest one $\mathbf{S_6}$.

to the computational cost associated with this method. Instead, we converted the binary file storing the equilibrium solution into a text file, padded it with an equal number of zeros on either side so as to extend the field in the localisation direction, and then reconverted it to a binary file. Finally we reconverged the new, larger field in the Newton solver. The new converged equilibrium solution was on the snake in the large domain and thus could be continued in Re to obtain new solutions on the snake. The results of the continuation can be seen in Figure 3-5 . This is the first computation of the equilibrium solutions on the snake for a large domain size. The positions of the right hand saddle-nodes on the bifurcation diagrams are given in Table 3-2.

3.3 Evidence of Oscillatory Behaviour

Solutions on the snake in both the large domain ($4\pi \times 2 \times 32\pi$) and the small domain ($4\pi \times 2 \times 16\pi$), when perturbed (by adding a small random field with $m = 10^{-4}$ and $s = 0.4$) and time integrated, exhibited oscillatory behaviour in their time evolution. The plots of dissipation, d, and L^2-norm of $\boldsymbol{u}$ clearly indicate some oscillations. The phase-space plots of the L^2-norms of the individual components of $\boldsymbol{u}$, provide further evidence of this oscillatory behaviour, which may be indicative of a periodic orbit. Time evolution and phase space plots of a sample solution on a positive-slope branch of the snake are show in Figure 3-6.

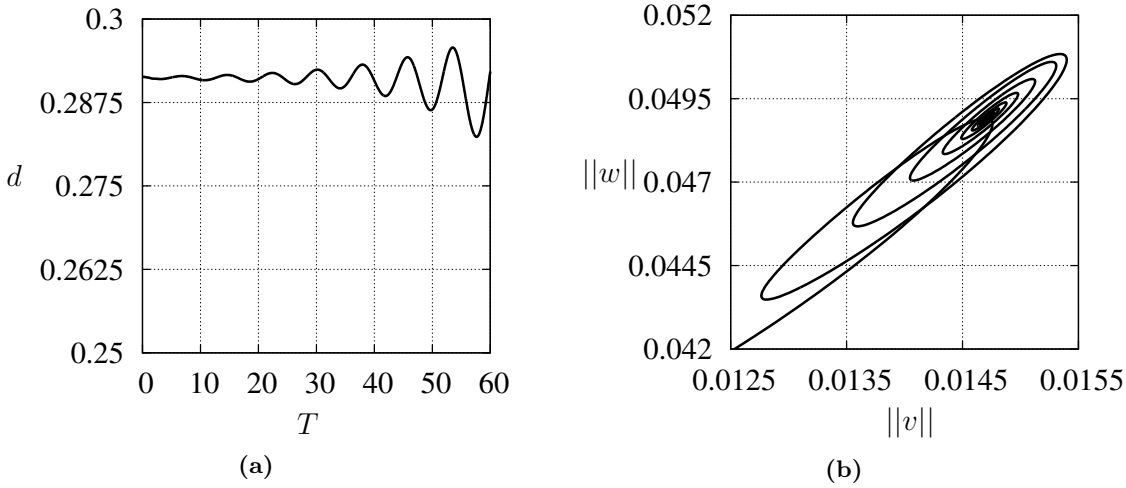

Figure 3-6: Oscillatory behaviour in the vicinity of the snake indicated by time evolution of the dissipation d of $\boldsymbol{u}$ (a) and oscillatory behaviour observed in the $||w|| - ||v||$ phase-space plot (b), for a solution on the snake at $Re = 171.9734$ and $D = 1.29134$.

More interesting is the fact that the amplitude of these oscillations seems to vary all along the snaking branch. Starting from the solution on the saddle-node $\mathbf{S_1}$, and moving down along the snake, the amplitude of oscillations decreases continuously, until the oscillations seem to disappear all together in the middle of negative slope branch. This behaviour could be due to the presence of a Hopf bifurcation [23, 24] somewhere along the snake. That would imply that there is a periodic orbit in the neighbourhood of the snake that is causing the oscillations.

Another possibility is that there is a collision of two leading eigenvalues along the branch. Before the collision, the solution has one leading eigenvalue with a zero imaginary part and another smaller eigenvalue which also has a zero imaginary part. After the collision, the two eigenvalues form a complex conjugate couple which may be responsible for the oscillatory behaviour observed in the vicinity of the snaking branch. The cause for the oscillations, whether it is the Hopf mode or the collision of eigenvalues or some other phenomenon needs to be investigated as it impacts the dynamics of the localised solutions in the neighbourhood of the snake.

3.4 Relaminarization

We carried out time-integration on the saddle-nodes for a domain size of $4\pi \times 2 \times 32\pi$ by perturbing these solutions to the right in parameter space, i.e., by increasing their Reynolds number, so as to determine whether a similar depinning transition is observed in the plane Couette configuration as in the one-dimensional Swift–Hohenberg equation. We used the saddle-nodes $\mathbf{S_0}, \mathbf{S_1}, \mathbf{S_3}$ as given in Table 3-2, to perform the time-integration and to evaluate the effect of moving up the snake. Contrary to our expectations, the solutions on all three saddle-nodes decayed to the laminar state, on slightly increasing ($\Delta Re = 0.01$) their Re and time-integrating. So we made finite value perturbations to the Re to observe the dynamics of the solutions on the right of the snake.

In order to study the dynamics of relaminarization, we computed the time (T^*) it takes for the initial solution on the saddle-node to reach a threshold value of the L^2-norm of the fluctuation velocity field $\boldsymbol{u}$, for different values of the Reynolds number on the right of each of the saddle-nodes.

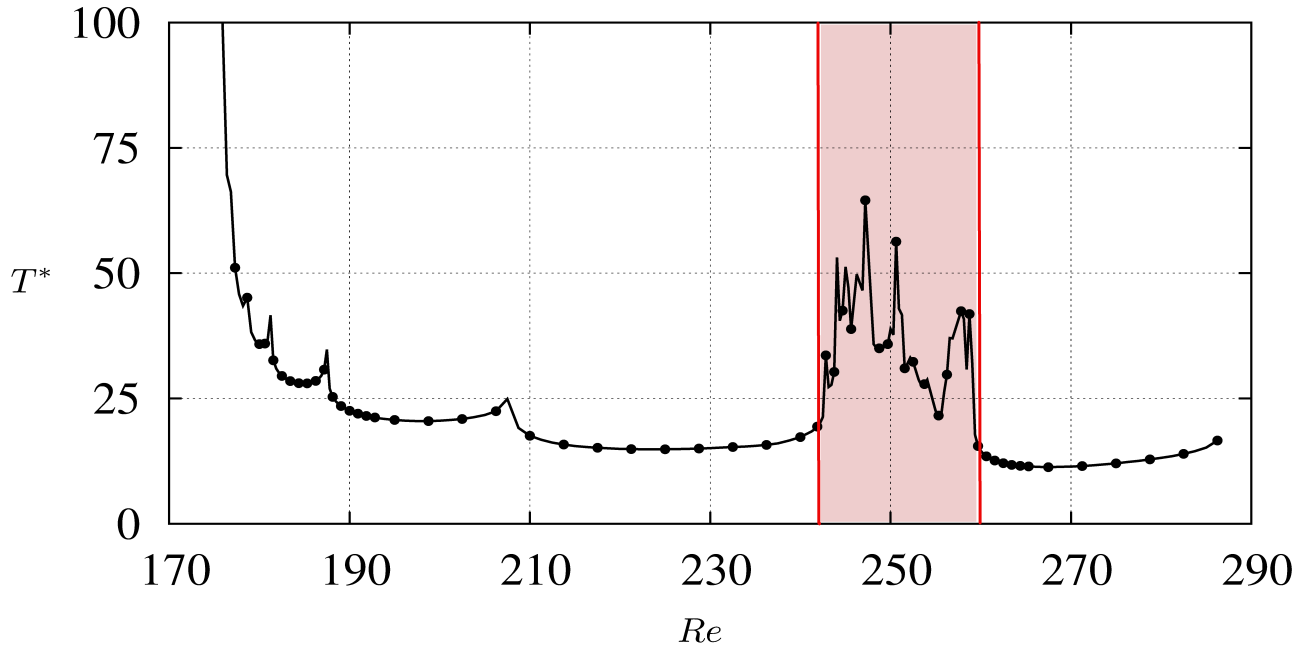

(a)

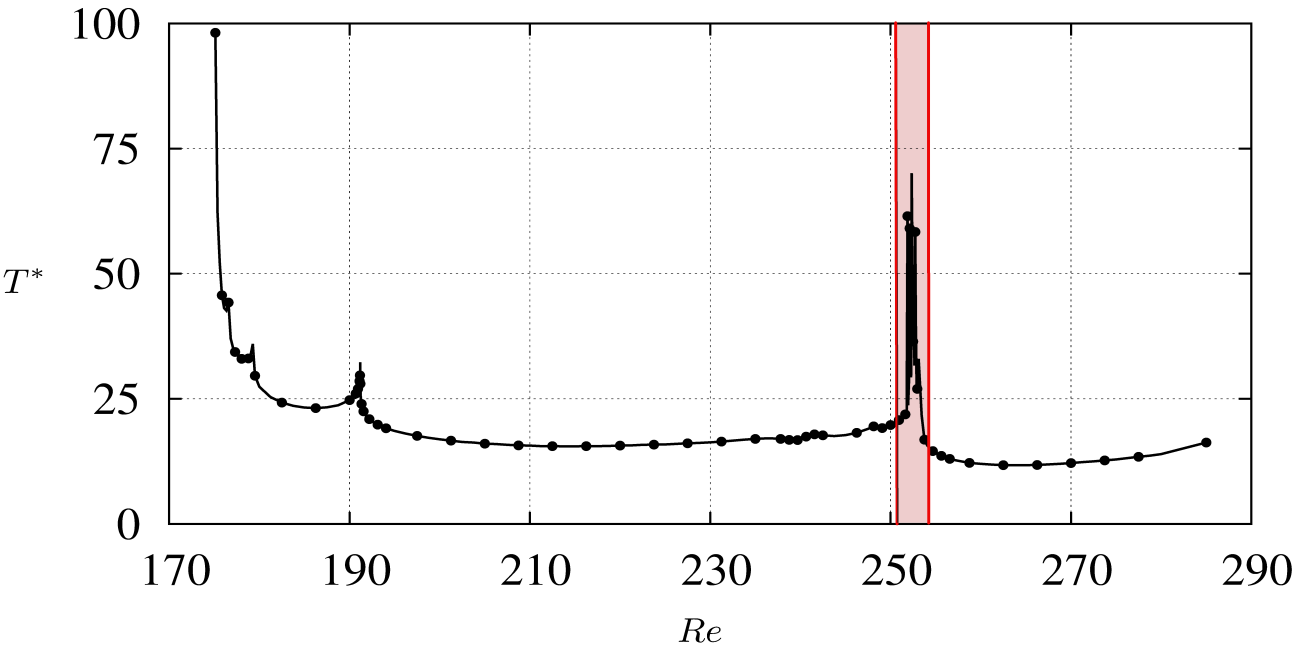

(b)

Figure 3-7: Time taken to reach an L^2-norm of 0.1 (T^*) as a function of Re for the saddle-node $\mathbf{S_0}$ (a) and the saddle-node $\mathbf{S_1}$ (b). The red lines demarcate the regime in which not all trajectories relaminarize (1 in every 3 data points is marked).

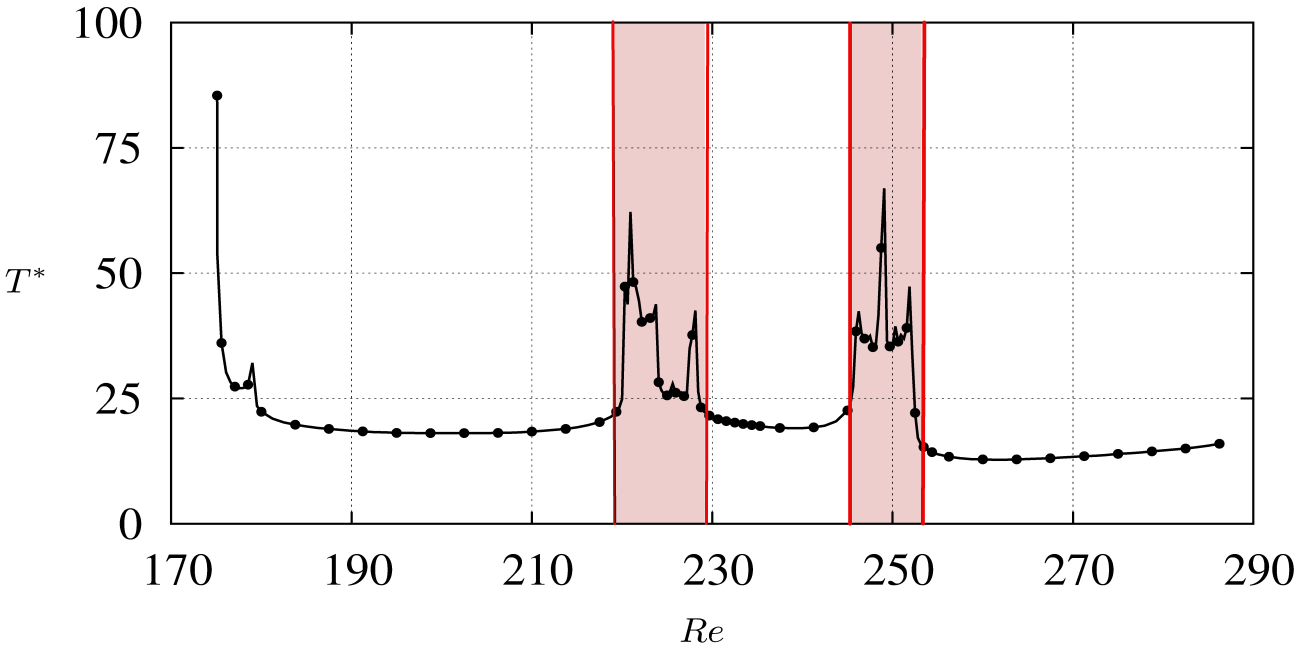

Figure 3-8: Time taken to reach an L^2-norm of 0.1 (T^*) as a function of Re for the saddle-node $\mathbf{S_3}$ (1 in every 3 data points is marked).

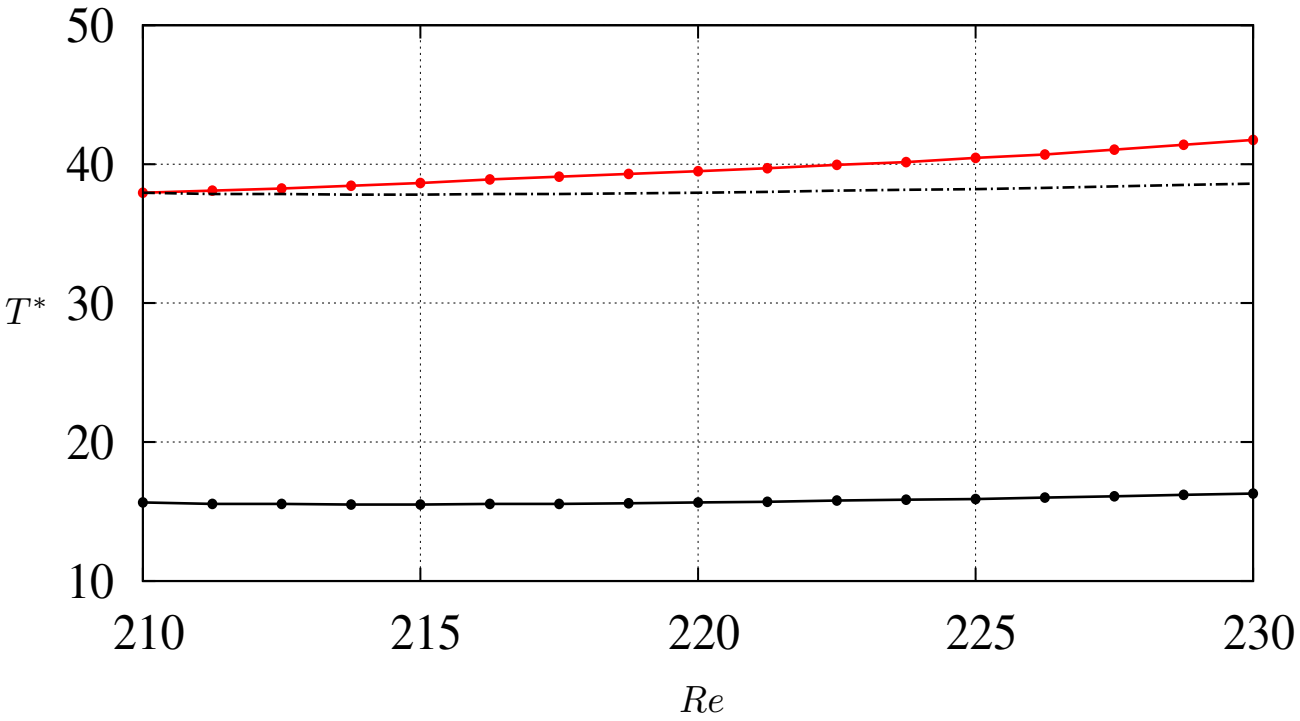

Figure 3-9: Effect of changing the L^2-norm threshold on the shape of the T^* vs. Re plot for the saddle-node $\mathbf{S_1}$, for $Re \in [210, 230]$. The solid line plots indicate the time to reach an L^2-norm of 10^{-1} (black) and 10^{-4} (red). The dashed line is the lower plot shifted upwards to indicate difference in slope between the two solid line plots. As the L^2-norm threshold is lower for the red plot, it is closer to the linear regime of the laminar flow and therefore attracted by its stable eigendirections. These directions, though stable for all Re, have decreasing growth rates with increasing Re, causing the solutions with higher Re to decay slower.

We chose the threshold value based on two factors, it should be well below the lower bound on the L^2-norm for turbulent trajectories beyond the transition Re and should be above the linear regime of the laminar state to prevent contamination by the stabilizing modes of the laminar state (their growth rates, though always negative, have a dependence on Re [25]). Based on these two factors the threshold was chosen to be 0.1. The solutions at the three saddle-nodes $\mathbf{S_0}, \mathbf{S_1}, \mathbf{S_3}$ were time-integrated at different Re above Re_{saddle}. The effect of Re on the time to the threshold L^2-norm, which we represent by T^*, is shown in Figure 3-7 and Figure 3-8. The effect of changing the threshold L^2-norm on form of the plot is shown in Figure 3-9. As can be seen in the figures, the plot of the T^* vs. Re seems to be mostly ordered before transition except for windows of pseudo-stochasticity, in which the T^* seems to be extremely sensitive to changes in the value of Re. Further refinement of these "windows" showed that there exist routes to chaos at specific Re. Thus, for both Figure 3-7 and Figure 3-8, the regimes demarcated by the red lines represent the stochastic parts of the plot. Here, we plot T^* only for the trajectories which decay to the laminar state. There exist trajectories in between which go to chaos and therefore cannot be represented on the plot. For example, the saddle-node $\mathbf{S_0}$, at $Re = 257.5$ (within the window), domain filling chaos was reached and sustained for at least 100 units of time. This is discussed further in Section 4.3 of the next chapter.

3.5 Transition and Front Propagation

The results shown in the previous section indicate that the presence of an exact transition Reynolds number for the localised solutions on the right-hand saddle-nodes is questionable. The traditional way to find the transition Re for a particular initial solution is to perform simple bisection between two Re, one at which the solution is known to relaminarize and another at which the solution is know to evolve into turbulence (sustained spatio-temporal chaos). Implicit in this method, however, is the assumption that there exists a Reynolds number threshold, beyond which a solution *always* goes to turbulence and below which it *always* relaminarizes. This is not true, as is clear from the existence of "windows", in the T^* vs. Re plots, which provide routes to chaos. Although, it still may be possible that there is a transition Re, before which *most* trajectories relaminarize and after which *all* trajectories go to turbulence. While time integrating the three saddle-node solutions to find the relaminarization time, we reached a particular Reynolds number beyond which it seemed that all the trajectories go to domain filling chaos. This gave us the impression that the previous statement might be true.

Initially, we did perform the bisection algorithm for the saddle-node $\mathbf{S_1}$. We bisected between an Re of 200 and 300. The decision to bisect upwards or downwards was taken based on the value of L^2-norm of the fluctuation velocity field $\boldsymbol{u}$ after 100 units of time. The threshold value was heuristically set to be 10^{-2}. The transition Re for the solution at the saddle-node $\mathbf{S_1}$ was found to be approximately 286.5. This approximate transition Re for all three saddle-nodes lies in the range of $280 - 290$. However on further refinement beyond this approximate transition Re, we found some trajectories which relaminarized. For the saddle-node $\mathbf{S_1}$, the solutions decayed back to the laminar state at Re as high as 395. Thus we must keep in mind that this is the transition Re beyond which *most* trajectories go to turbulence (domain-filling chaos) and before which *most* trajectories relaminarize. In fact, our results show that the bisection algorithm we ran may have failed, due to the absence of an exact value for the transition Re. This shows that the correct way to deal with transition, even for just one initial condition, is probabilistically.

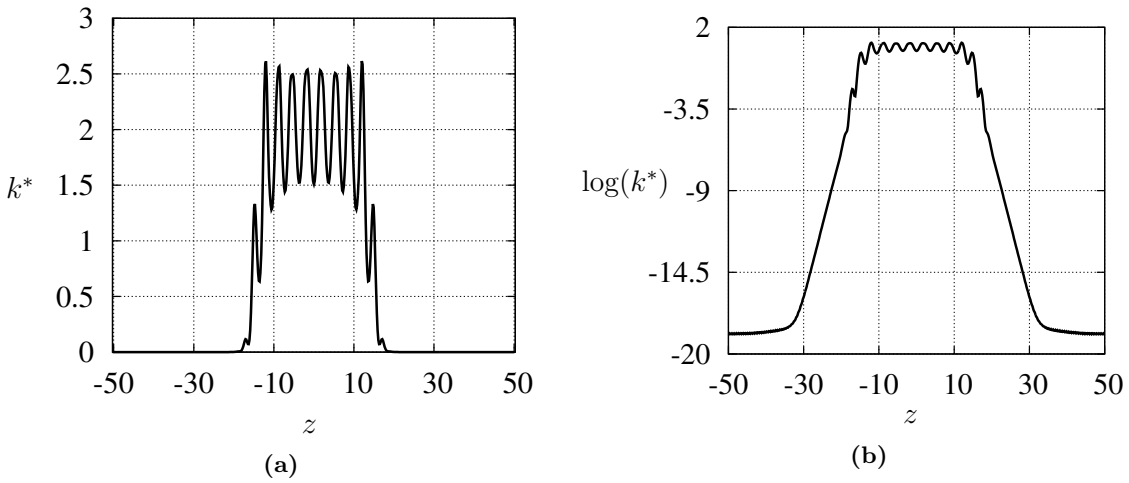

Figure 3-10: (a). k^* vs. z plot for the saddle-node $\mathbf{S_1}$ (b). $\log(k^*)$ vs. z for the saddle-node $\mathbf{S_1}$. A threshold value of 10^{-2}, is used to determine the position of the front.

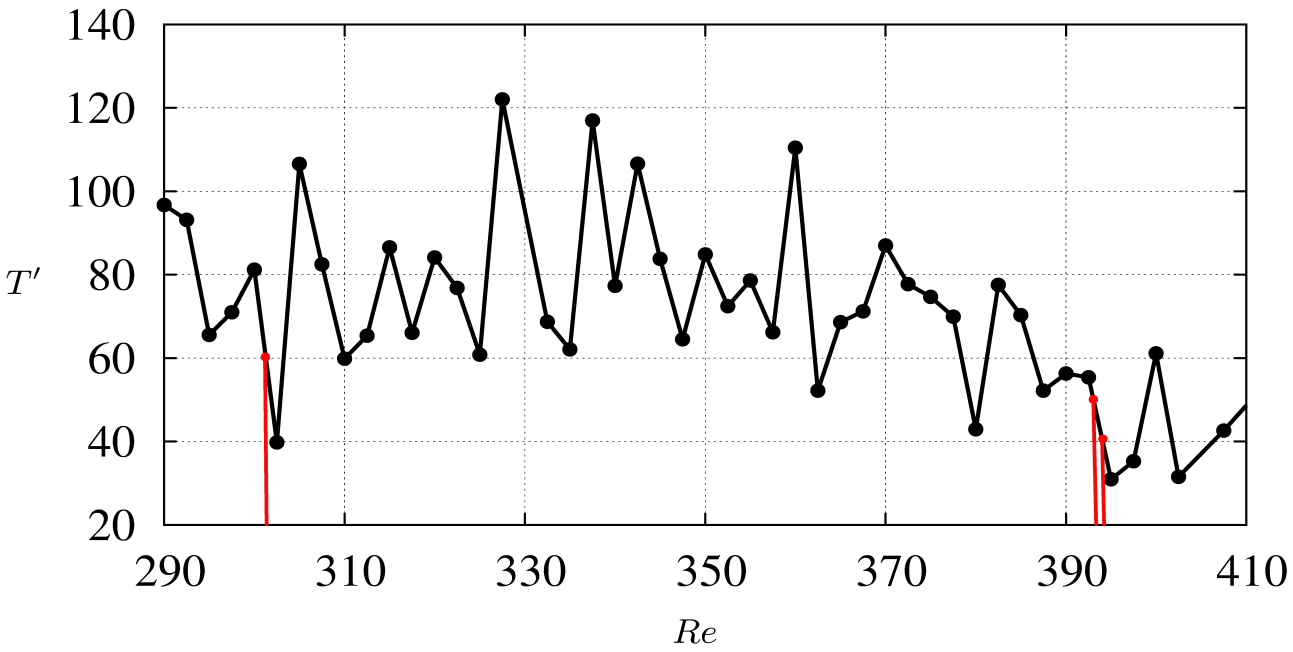

Figure 3-11: Time taken to for the solution/pattern to reach a length of 80 ($T^{'}$) vs. Reynolds number. The length is obtained by subtracting the location of the left front from that of the right front. The points in red indicate solutions that decay to the laminar state.

As mentioned earlier, we are interested in the dynamics of the fronts of the localised solution. In order to compute where the front of the localised solution is located we need to calculate some z-dependent (z being the localization direction) integral quantity. We chose to compute the fluctuation kinetic energy of the velocity field at every point. This quantity was then integrated over the x and y directions to get a z-dependent quantity which we represent by $k^*(z) = \int\int \frac{1}{2}||\boldsymbol{u}||^2(x, y, z)dxdy$. The plot of k^* vs. z for the localised solution on the saddle-node $\mathbf{S_1}$ is shown in Figure 3-10. In order to find the position of the solution's front, we checked for the z coordinate (on the left and right sides) at which k^*, first exceeded a threshold value of 10^{-2}. Since the data is stored in a discrete vector, we interpolated this position with the neighbourhood points, which gave us an approximate front location. From the left and right front locations we computed the length of the pattern by subtracting the two. Starting from $Re = 290$, which we know is above the approximate Re after which domain-filling chaos becomes frequent, we time integrated the solution on the saddle-node $\mathbf{S_1}$ at different Re till $Re = 400$. For all the solutions that transitioned to domain-filling chaos, we checked the time taken for the pattern to reach a length of 80 (79.58 % of L_z). We represent this quantity by T'. We did not choose the threshold as the full domain size because as the front gets closer to the edges of the domain, domain size effects kick in and affect the dynamics of the front. The plot of T' vs. Re for the solution on the saddle-node $\mathbf{S_1}$ can be seen in Figure 3-11. It can be seen from the plot that the dynamics of front propagation are essentially chaotic. The dependence of T' on Re seems to be more or less arbitrary. An ordered dependence of the front propagation on Re for the Swift–Hohenberg equation as can be seen in [26], does not seem to carry over for the Navier–Stokes equations.

4 Discussion and Conclusions

4.1 Suppression of Depinning

Time integration of the three saddle-node solutions showed that the depinning mode present in the Swift–Hohenberg equation is either absent or suppressed in the plane Couette flow configuration. The difference in the dynamics may lie in the fact that the spatially periodic Nagata solution is unstable in the vicinity of the pinning region [16], while the upper branch of the patterned solutions of the Swift–Hohenberg equation is stable in the vicinity of the pinning region. The spatially periodic Nagata solution is known to have unstable amplitude-killing modes. Since the localised solutions on the snake in plane Couette flow are formed by placing a front between the trivial state and the Nagata solution, we conjecture that they possess the same amplitude killing mode. This mode may be suppressing the depinning mode. A rigorous numerical linear stability analysis in small or large domains, attesting to the presence of this mode, is yet to be performed.

Another explanation is the oscillatory behaviour observed near the snaking branch. These oscillations may either be the leading direction along the unstable manifold which leads to relaminarization or be due to the influence of a nearby periodic orbit. In the latter case, the periodic orbit may be attracting the localised solution when it is perturbed. The solutions first oscillates while increasing in amplitude. As it approaches the periodic orbit, its component along the unstable direction of the periodic orbit increases, causing it to move along the periodic orbits unstable manifold and relaminarize. To show this one would have to first find the periodic orbit and continue it to find the entire branch of solutions. Both the amplitude-killing mode and the periodic orbit's influence may be responsible for the suppression of the depinning mode, if present.

In order to try and isolate the depinning mode, we modified the time-stepping to readjust the L^2-norm of the field every timestep as follows,

$$\mathbf{u_m} = \mathbf{u_{new}} * \frac{||\mathbf{u_i}||}{||\mathbf{u_{new}}||} \tag{4-1}$$

where $\mathbf{u_m}$ is the modified field, $\mathbf{u_{new}}$ is the field obtained every time-step and $\mathbf{u_i}$ is the initial field at $t = 0$. By doing this, we aimed to suppress the amplitude killing mode in hopes that we would observe depinning. However, the depinning was not observed and the solution simply decayed to the laminar state. A more advanced technique will be needed to isolate this depinning mode, if at all it is present.

4.2 Jumps in the T^* vs. Re Plots

Figure 3-7 and Figure 3-8 show a number of sudden jumps in the value of T^*, before the"windows" of chaos, for all three saddle-nodes $\mathbf{S_0}$, $\mathbf{S_1}$ and $\mathbf{S_3}$. The explanation for these jumps stems, once again, from the oscillatory behaviour observed near the snaking branch. Take for example the second jump T^* vs. Re plot of the saddle-node $\mathbf{S_1}$, which occurs at $Re \simeq 191.2$. An enlarged version of the jump can be seen in Figure 4-1a. It can be seen there is sudden increase in T^* followed by a sudden drop. If we consider three values of Re, one to the left of the jump, one to the right and one at the peak,

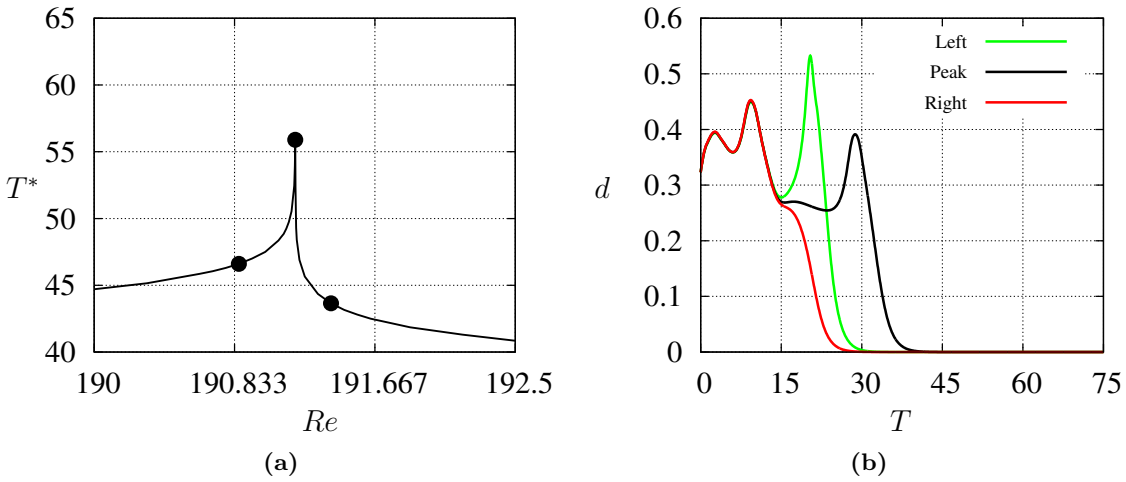

Figure 4-1: (a) T^* vs. Re showing the jump in the value of T^*. The three points indicated have Reynolds numbers $Re_1 = 190.859375$ to the left of the peak, $Re_2 = 191.193359$ on the peak, and $Re_3 = 191.406250$ to the right of the peak. (b) d vs. T plot for the three points near the jump, to the left (green), on the peak (black) and on the right (red).

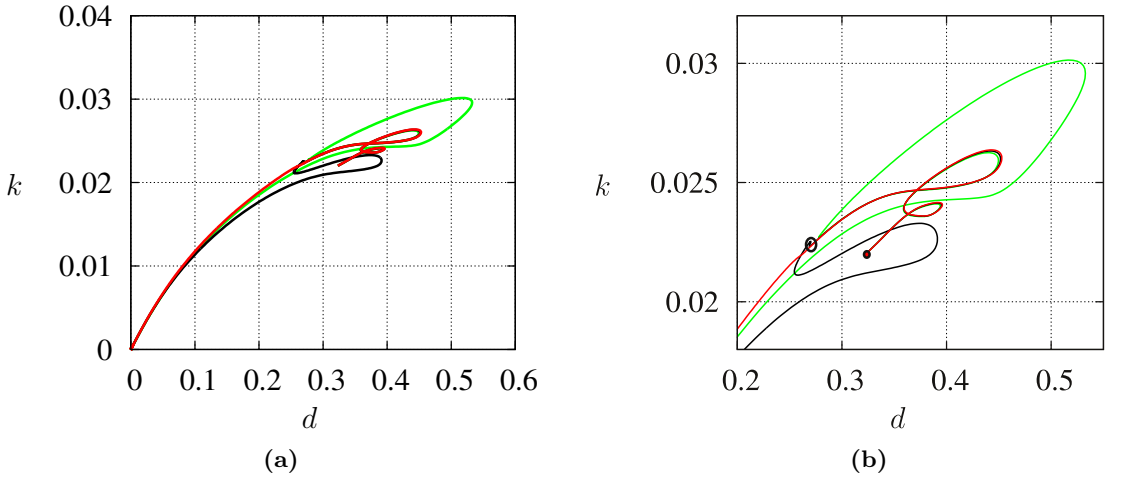

Figure 4-2: (a) Fluctuation kinetic energy k vs. fluctuation dissipation d phase space plot for the three trajectories - left of the jump (green), on the peak (black) and right of the jump (red). (b) k vs. d (zoomed in) plot showing the initial oscillatory behaviour that occurs before decay.

we can try and understand the cause of this behaviour. Further insight as to what happens can be gained by looking at the time evolution and phase space plots of the three different points. The plots of the dissipation of the fluctuation field d vs. time can be seen in Figure 4-1b. As can be seen in the figure, the solutions both to the left (green) and the right (red) of the peak perform oscillations. This oscillatory behaviour is expected as it was observed when solutions on the snaking branch were perturbed and time-integrated. As we discussed earlier, the reason for the oscillations could either be the presence of a nearby periodic orbit coming from a Hopf bifurcation on the branch or a collision of two large eigenvalues forming a complex conjugate couple and producing an oscillatory instability.

It can be clearly observed in Figure 4-1b that the solution to the left performs one more oscillation than the solution to the right of the peak. In the case of the presence of a Hopf mode, this could be the case of the periodic orbit branch becoming more unstable with increasing Re. As a result, the solution to the right is pushed towards the unstable manifold of the periodic orbit faster and so performs one less cycle. A clearer picture of the dynamics can be obtained by looking at the plot of

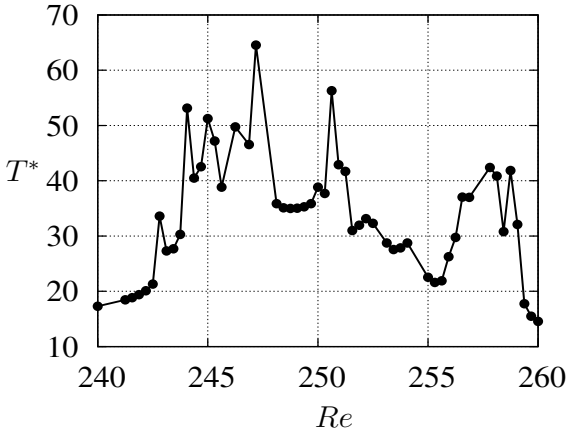

Figure 4-3: Unordered/pseudo-stochastic region of the T^* vs. Re plot for the saddle-node $\mathbf{S_0}$ for $Re \in [240, 260]$. In this region or "window" T^* is extremely sensitive to small changes in Re. If looked at closely, one can see a region of order between two patches of chaos. The dearth of data points in some parts of the plot is due to the fact that a number of trajectories in this zone transition to turbulence and so never reach an L^2-norm of 0.1.

d vs. $k = \frac{1}{2V}\int_\Omega ||\boldsymbol{u}||^2 d\Omega$, the fluctuation kinetic energy in Figure 4-2. The enlarged version of the plot can be seen in Figure 4-2b. The point where the three trajectories separate has been encircled in black while the initial condition (same for all three) has been circled in red. It can be seen that at the point where the three trajectories separate, the trajectory to the left of the peak (green) performs an additional loop in $d-k$ space, while the trajectory to the right (red) decays to zero monotonically. The trajectory at the peak itself (black) seems to be a transitional one between the three-loop and two-loop trajectories. It doesn't complete a third loop but neither does it decay monotonically. Instead it moves to some other part of $d-k$ space causing it to decay slower than both the three-loop and two-loop trajectories. We believe that these jumps are transitions from $(N+1)$-loop to (N)-loop oscillatory behaviour.

4.3 Windows of Chaos in the T^* vs. Re Plots

The T^* vs. Re plots for all three saddle-nodes $\mathbf{S_0}$, $\mathbf{S_1}$, and $\mathbf{S_3}$, have at least one region where the T^* is extremely sensitive to changes in Re. The value of T^* seems to fluctuate arbitrarily within this region of the plot and has the semblance of being random. An enlarged version of this region of the plot for the saddle-node $\mathbf{S_0}$ can be seen in Figure 4-3. As mentioned earlier, on further refinement, it was observed that a number of trajectories transitioned to turbulence. For the solution on the saddle-node $\mathbf{S_0}$, time integrated at $Re = 257.5$, domain filling chaos was obtained after approximately 175 units of time and was sustained for at minimum 100 units of time. This is shown in Figure 4-4. The arbitrary nature of the T^* plot can be attributed to the fact that in this subset of the Reynolds number the intersections of the stable manifolds of the laminar state, the turbulent state and other fixed points/periodic orbits of the system are extremely sensitive to a change in the Reynolds number. This is explained in Figure 4-5. If initially a solution lies on the stable manifold of the laminar state, a small change in the Re causes it to lie on the stable manifold of some other fixed point. Once it reaches this fixed point it may destabilize and reach the laminar state. The presence of turbulent trajectories indicates that for certain Re, the initial condition lies on the stable manifold of the turbulent state. As a result it is attracted towards the turbulent state and transitions to domain filling chaos.

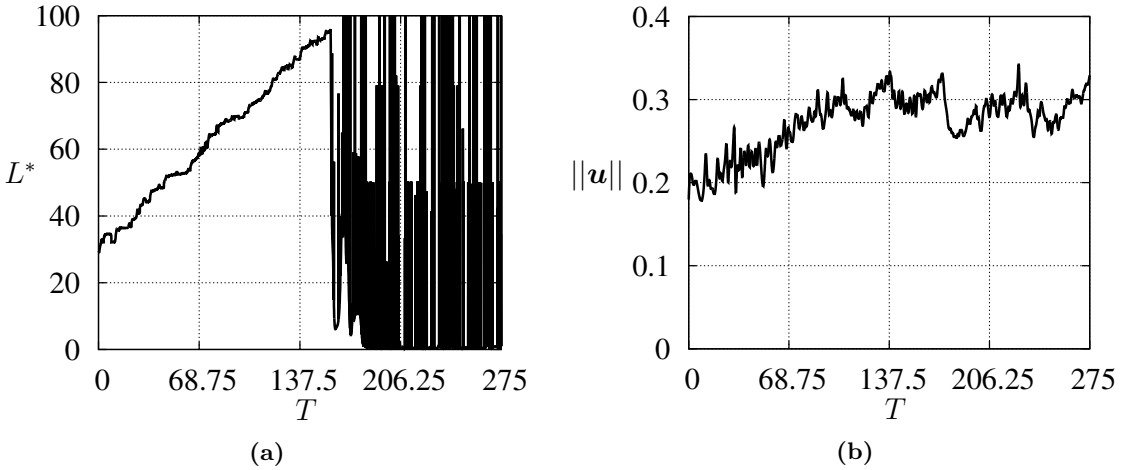

Figure 4-4: Time evolution of pattern size, L^* (a) and $||\boldsymbol{u}||$ (b), at $Re = 257.5$ for the solution at the saddle-node $\mathbf{S_1}$. The pattern size fills the domain at $T \simeq 175$ units of time. After the pattern fills about 85 % of the domain, domain size effects seem to kick in. Beyond this, the definition of the front of the solution is no longer valid.

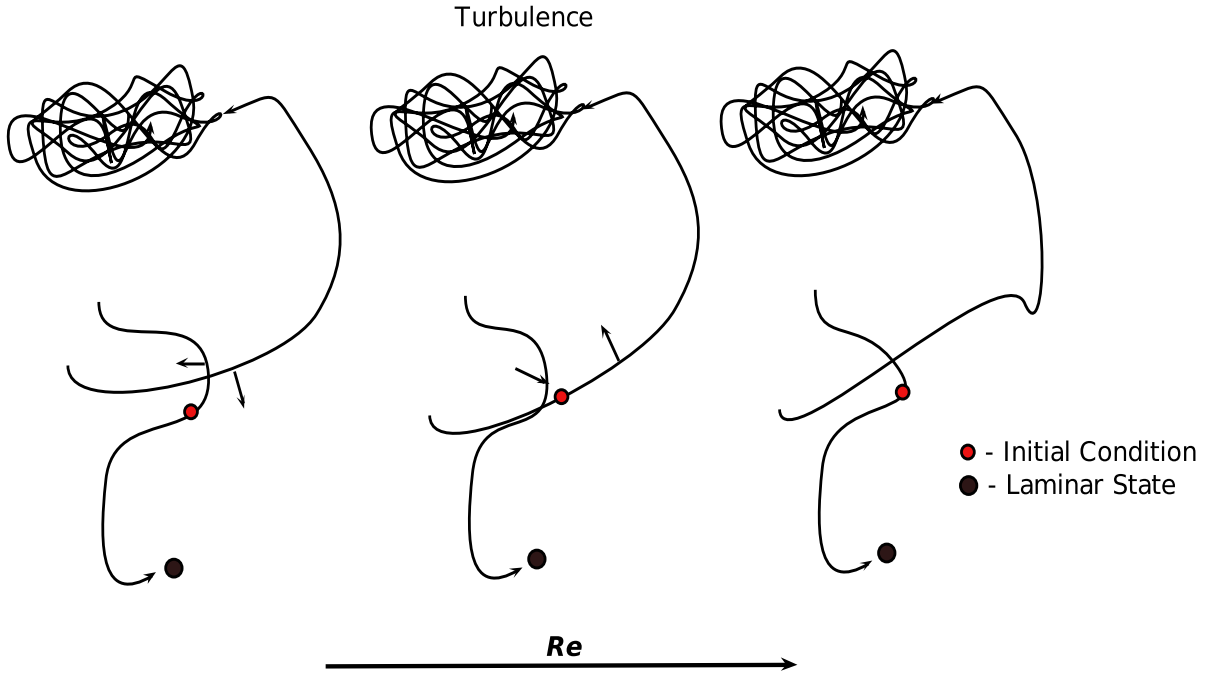

Figure 4-5: Intersections of the stable manifolds of different stationary states and attractors in the dynamical system are sensitive to changes in Re within the "window". As the Re is changed the manifolds reorient (shown by the direction of the arrows), causing the initial condition to behave differently. Initially the solution lies on the stable manifold of the laminar state. A small change in Re causes it to lie on the stable manifold of the turbulent state. Further changes in Re, may cause it to return to the stable manifold of the laminar state but at a different location.

4.4 Nature of Transition

The results pertaining to both relaminarization and front propagation show that a fixed transition Re below which all trajectories relaminarize and above which all trajectories go to turbulence does not exist. In the case of relaminarization, all three saddle-nodes exhibited windows which provided routes to domain filling chaos. After $Re = 290$, beyond which most trajectories went to domain filling chaos, there still existed trajectories which decayed to the laminar state, in particular - the solution at the saddle-node $\mathbf{S_1}$ decayed to the laminar state at $Re = 395$. This shows that the correct way to treat transition is probabilistically rather than deterministically. The fact that transition is not well-defined for the localised solutions seems to contradict the results found in [21, 20]. We have shown that domain filling chaos is obtained at lower Re than 325 for a specific initial condition. Although these studies, treated transition using mean growth and decay times for a range of initial conditions, our results seem to show that even for specific initial conditions (the localised solutions on the snake), the transition Re is not well-defined.

4.5 Stochastic Nature of Front Propagation

The results from the previous chapter indicate that the front motion is essentially stochastic/chaotic. These results are confirmed by those of Duguet *et. al* [27]. They showed that the motion of the interface between a turbulent puff and a laminar background is stochastic. We have shown the same for localised solutions as initial conditions. This indicates that the stochastic motion of the front may be a property of the system rather than of the initial condition used. A more thorough treatment, using a Markov chain process to model the front motion like that used in [27] is possible.

4.6 Future Scope

Given the results we have obtained there are a number of new avenues we would wish to pursue in the future. It would definitely be interesting to investigate the phenomenon causing the transition in the stochastic "windows". Could it be possible that a crises bifurcation-like the scenario observed by Zammert and Eckhardt [28] for pipe flow is responsible for this sudden burst of chaos? Or could it be something more well-known like a period doubling bifurcation caused by the Hopf mode (if present)?

Further, it would be interesting to carry out a numerical linear stability analysis on the snaking branch to isolate the modes playing a major role in its dynamics. This may indicate if a there is a periodic orbit in the neighbourhood of the branch.

Since the localised solutions are obtained by continuing an edge state at $Re = 400$, it would interesting to see if these results and related dynamics carry over to the edge states at different Reynolds numbers (considering their critical role in transition to turbulence).

References

[1] J. Burke and E. Knobloch, Localized states in the generalized Swift–Hohenberg equation, *Phys. Rev. E.* **73**, 056211 (2006).

[2] S. Fauve and O. Thual, Solitary waves generated by subcritical instabilities in dissipative systems, *Phys. Rev. Lett.* **64**, 282 (1990).

[3] T. M. Schneider, J. F. Gibson, M. Lagha, F. D. Lillo, and B. Eckhardt, Laminar-turbulent boundary in plane Couette flow, *Phys. Rev. E* **78**, 037301 (2008).

[4] T. M. Schneider, D. Marinc, and B. Eckhardt, Localized edge states nucleate turbulence in extended plane Couette cells, *J. Fluid. Mech.* **646**, 441 (2010).

[5] Y. Duguet, P. Schlatter, and D. S. Henningson, Localized edge states in plane Couette flow, *Phys. Fluids* **21**, 111701 (2009).

[6] S. Grossmann, The onset of shear flow turbulence, *Rev. Mod. Phys.* **72**, 603 (2000).

[7] J. D. Skufca, J. A. Yorke, and B. Eckhardt, Edge of Chaos in a Parallel Shear Flow, *Phys. Rev. Lett.* **96**, 174101 (2006).

[8] N. Tillmark and P. Alfredsson, Experiments on transition in plane Couette flow, *J. Fluid Mech.* **235**, 89 (1992).

[9] T. M. Schneider, J. F. Gibson, and J. Burke, Snakes and Ladders: Localized Solutions of Plane Couette Flow, *J. Fluid Mech.* **104**, 104501 (2010).

[10] S. H. Strogatz, *Nonlinear dynamics and chaos : with applications to physics, biology, chemistry, and engineering*, (Westview Press 2014), 2nd edition.

[11] K. Kirchgässner, Wave-solutions of reversible systems and applications, *J. Diff. Eq.* **45**, 113 (1982).

[12] Y. Pomeau, Front motion, metastability and subcritical bifurcations in hydrodynamics, *Physica D* **23**, 3 (1986).

[13] M. Beck, J. Knobloch, D. J. B. Lloyd, B. Sandstede, and T. Wagenknecht, Snakes, Ladders, and Isolas of Localized Patterns, *SIAM J. Math. Anal.* **41**, 936 (2009).

[14] P. Coullet, C. Riera, and C. Tresser, Stable Static Localized Structures in One Dimension, *Phys. Rev. Lett.* **84**, 3069 (2000).

[15] D. Avitabile, D. J. B. Lloyd, J. Burke, E. Knobloch, and B. Sandstede, To Snake or Not to Snake in the Planar Swift–Hohenberg Equation, *SIAM J. Appl. Dyn. Syst.* **9**, 704 (2010).

[16] M. Nagata, Three-dimensional finite-amplitude solutions in plane Couette flow: bifurcation from infinity, *J. Fluid Mech.* **217**, 519 (1990).

[17] J. F. Gibson, Channelflow: A spectral Navier-Stokes simulator in C++, Technical report, U. New Hampshire (2014), `Channelflow.org`.

[18] D. Viswanath, Recurrent motions within plane Couette turbulence, *J. Fluid Mech.* **580**, 339 (2007).

[19] C. Beaume, An adaptive preconditioner for continuation of incompressible flows, In Preparation.

[20] O. Dauchot and F. Daviaud, Finite amplitude perturbation and spots growth mechanism in plane Couette flow, *Phys. Fluids* **7**, 335 (1995).

[21] L. Shi, M. Avila, and B. Hof, Scale Invariance at the Onset of Turbulence in Couette Flow, *Phys. Rev. Lett.* **110**, 204502 (2013).

[22] D. Barkley and L. S. Tuckerman, Computational study of turbulent laminar patterns in couette flow, *Phys. Rev. Lett.* **94**, 014502 (2005).

[23] L. Perko, *Differential Equations and Dynamical Systems*, (Springer, New York ; London 2001), 3rd edition.

[24] F. Charru, *Hydrodynamic Instabilities*, (Cambridge University Press 2011).

[25] P. J. Schmid and D. S. Henningson, *Stability and Transition in Shear Flows*, (Springer, New York, NY 2012), 1st edition.

[26] P. Gandhi, C. Beaume, and E. Knobloch, A New Resonance Mechanism in the Swift–Hohenberg Equation with Time-Periodic Forcing, *SIAM J. Appl. Dyn. Syst.* **14**, 860 (2015).

[27] Y. Duguet, O. L. Maître, and P. Schlatter, Stochastic and deterministic motion of a laminar-turbulent front in a spanwisely extended Couette flow, *Phys. Rev. E* **84**, 066315 (2011).

[28] S. Zammert and B. Eckhardt, Crisis bifurcations in plane Poiseuille flow, *Phys. Rev. E.* **91**, 041003 (2015).